

FluxNet: Learning Capacity-Constrained Local Transport Operators for Conservative and Bounded PDE Surrogates

Zishuo Lan¹ Junjie Li¹ Lei Wang¹ Jincheng Wang¹

Abstract

Autoregressive learning of time-stepping operators offers an effective approach to data-driven PDE simulation on grids. For conservation laws, however, long-horizon rollouts are often destabilized when learned updates violate global conservation and, in many applications, additional state bounds—such as nonnegative mass and densities or concentrations constrained to $[0, 1]$. Enforcing these coupled constraints via direct next-state regression remains difficult. We introduce a framework for learning conservative transport operators on regular grids, inspired by lattice Boltzmann-style discrete-velocity transport representations. Instead of predicting the next state, the model outputs local transport operators that update cells through neighborhood exchanges, guaranteeing discrete conservation by construction. For bounded quantities, we parameterize transport within a capacity-constrained feasible set, enforcing bounds structurally rather than by post-hoc clipping. We validate FluxNet on 1D convection-diffusion, 2D shallow water equations, 1D traffic flow, and 2D spinodal decomposition. Experiments on shallow-water equations and traffic flow show improved rollout stability and physical consistency over strong baselines. On phase-field spinodal decomposition, the method enables large time-steps with long-range transport, accelerating simulation while preserving microstructure evolution in both pointwise and statistical measures.

1. Introduction

Autoregressive neural surrogates for partial differential equations (PDEs) offer a promising approach for accelerating scientific simulations. By learning a time-stepping operator

from data, these models can replace expensive numerical solvers with fast neural network inference. However, when deployed for long-horizon rollouts, a fundamental challenge arises: errors compound over time, leading to predictions that violate basic physical laws.

Many physical systems are governed by conservation laws—the total mass, momentum, or energy in a closed system remains constant over time. Additionally, the conserved quantities often have physical bounds: concentrations cannot be negative, densities cannot exceed saturation limits, and water depths must remain nonnegative. Standard neural network architectures provide no structural guarantee for either property. As a result, autoregressive rollouts frequently exhibit conservation drift, where the global sum of conserved quantities gradually deviates from its initial value, and bound violations, where predicted values exceed physically valid ranges such as negative concentrations or densities greater than unity.

Existing approaches address these issues through either soft constraints or post-hoc corrections. Soft constraints add penalty terms to the loss function (Raissi et al., 2019) but cannot guarantee satisfaction at test time, and errors continue to accumulate during rollout—a phenomenon analogous to exposure bias in sequence modeling, where training-time and rollout-time distributions diverge (Bengio et al., 2015; Ross et al., 2011). Post-hoc projection can enforce constraints; indeed, projecting each update onto the feasible set can eliminate drift in principle (Singha, 2025), but such corrections can alter local transport structure or introduce order-dependent artifacts when applied to multi-field systems. We observe that both conservation and boundedness can be viewed through the lens of feasible transport. Physical transport of conserved quantities is inherently local: mass moves between neighboring regions, not teleporting across the domain. Furthermore, the amount transported is constrained by what the sender has available and what the receiver can accommodate.

This perspective motivates our approach: instead of learning to predict the next state directly, we learn a capacity-constrained local transport operator. The network outputs a transport plan—fluxes between neighboring cells—that respects feasibility constraints by construction. A subse-

¹State Key Laboratory of Solidification Processing, Northwestern Polytechnical University, Xi'an, 710072, China. Correspondence to: Junjie Li <lijunjie@nwpu.edu.cn>, Jincheng Wang <jchwang@nwpu.edu.cn>.

quent conservative update, which simply tallies outflows and inflows, produces the next state with guaranteed conservation and, for appropriate head designs, guaranteed or near-guaranteed bound satisfaction. We instantiate this idea through FluxNet, a family of transport heads that parameterize feasible local transport plans. Conservation is achieved structurally since the same flux serves as outflow for the sender and inflow for the receiver. Lower bounds are enforced by parameterizing outflow as a fraction of the available amount above the bound via the L-head, upper bounds are enforced through the U-head’s capacity-limited inflow, and dual bounds are addressed by combining both perspectives with a consistency regularizer in the D-head, achieving near-zero violations empirically. The tunable stencil radius enables effective large-timestep modeling by accommodating longer-range transport.

We validate FluxNet on four diverse conservative PDE benchmarks spanning different physics and constraint types: 1D convection-diffusion with lower-bounded concentration, 2D shallow water equations with coupled mass-momentum conservation and nonnegative depth constraints, 1D traffic flow with dual-bounded density featuring shocks and rarefaction waves, and 2D spinodal decomposition with dual-bounded phase field requiring statistical fidelity. Across all benchmarks, FluxNet achieves machine-precision conservation, reduced bound violations, and improved long-rollout accuracy compared to direct regression baselines and soft-constraint methods.

2. Related Work

2.1. Neural Operators and Long-Horizon Rollout Stability

Neural operators provide a data-driven approach to learning solution operators of partial differential equations. The Fourier Neural Operator parameterizes integral kernels in Fourier space, enabling resolution-invariant learning for a broad class of PDEs (Li et al., 2020). Physics-informed DeepONets extend operator learning with PDE residual constraints (Wang et al., 2021). Message-passing neural PDE solvers leverage graph neural networks (Gilmer et al., 2017; Battaglia et al., 2018) to handle unstructured meshes (Brandstetter et al., 2022; Pfaff et al., 2020), while multi-scale approaches address varying spatiotemporal resolutions (Gupta & Brandstetter, 2022). Machine learning has also accelerated traditional CFD solvers (Kochkov et al., 2021). However, these architectures do not inherently enforce physical conservation laws, potentially leading to drift in conserved quantities during long rollouts (Li et al., 2022). To mitigate distributional shift in autoregressive prediction, strategies such as scheduled sampling in sequence models (Bengio et al., 2015; Ross et al., 2011) and pushforward training (Brandstetter et al., 2022; Sanchez-Gonzalez et al., 2020)

have been explored, improving stability by exposing models to their own predictions during training. While these techniques reduce error accumulation, they provide no formal guarantees on conservation or solution boundedness. Even recent long-rollout surrogates such as PDE-Refiner (Lippe et al., 2023) focus on reducing error growth via refinement, without enforcing strict conservation laws.

2.2. Flux-Based Conservative Neural Surrogates

Embedding conservation structure directly into neural network architectures offers a principled alternative to soft regularization. FINN draws inspiration from finite volume methods, learning flux functions that respect the divergence form of conservation laws (Praditia et al., 2021; Karlbauer et al., 2022). Physics-embedded neural networks extend this to handle mixed boundary conditions (Horie & Mitsume, 2022). Other approaches enforce entropy stability in neural flux-form models (Liu et al., 2025). Energy-based formulations provide another route to structure-preserving dynamics (Matsubara et al., 2020). Our work shares the philosophy of flux-based parameterization but differs in several key aspects: we target regular grids with configurable stencil radii enabling larger effective time steps through expanded spatial support, and more fundamentally, we integrate boundedness constraints directly into the conservation-feasible region, ensuring that learned fluxes simultaneously preserve both total mass and solution bounds.

2.3. Positivity and Bound Preservation

Positivity preservation and boundedness are classical concerns in computational physics, where violations can cause numerical instability or unphysical solutions. Traditional numerical schemes achieve positivity and boundedness through careful limiter design or convex combinations (Van Leer, 1979; Zhang & Shu, 2010), with finite volume methods providing a natural framework (LeVeque, 2002). In machine learning approaches, boundedness is typically enforced via penalty terms, output clipping, or sigmoid squashing. However, such strategies interact poorly with autoregressive rollout: small violations accumulate over time, eventually producing catastrophic errors (Liu et al., 2025). Our feasible-set transport head provides a structural guarantee by construction, ensuring every predicted flux yields bounded updates regardless of the learned parameters.

2.4. LBM-Inspired Stencil Channelization

The Lattice Boltzmann Method (LBM) discretizes velocity space into a finite set of directions, evolving distribution functions along each channel independently before local collision (Timm et al., 2016). We borrow only the stencil-channelization concept: our flux network parameterizes directional fluxes as separate channels corresponding to

neighbor directions in the computational stencil, facilitating interpretable direction-aware flux prediction without imposing specific collision dynamics.

3. Method

3.1. Problem Setup

We consider conservative PDE dynamics discretized on regular periodic grids. Let the state at discrete time t be $\mathbf{u}^t \in \mathbb{R}^{C \times H \times W}$ (or $C \times L$ in 1D), where each channel represents a conserved quantity such as concentration, density, or momentum. Given optional external fields ϕ (e.g., velocity fields, material parameters), our goal is to learn an autoregressive surrogate operator \mathcal{T}_θ that maps the current state to the next:

$$\mathbf{u}^{t+1} = \mathcal{T}_\theta(\mathbf{u}^t, \phi), \quad (1)$$

which is then rolled out for long-horizon prediction. A fundamental difficulty with standard neural surrogates that directly predict \mathbf{u}^{t+1} is twofold: conservation drift accumulates errors in global conserved quantities over long rollouts, and bound violations produce values that exceed physically valid ranges. We address both issues by changing the learned object: instead of predicting the next state directly, we predict a local transport plan and perform a structurally conservative update.

3.2. Conservative Transport Update

Let $\mathcal{N}(i)$ denote the neighborhood of grid cell i defined by a fixed stencil on the periodic grid. We parameterize a directed transport amount $F_{i \rightarrow j}$ representing the quantity transferred from cell i to cell j in one surrogate step. The state update follows:

$$u_i^{t+1} = u_i^t - \sum_{j \in \mathcal{N}(i)} F_{i \rightarrow j} + \sum_{j \in \mathcal{N}(i)} F_{j \rightarrow i}. \quad (2)$$

On regular grids, we parameterize fluxes per directional offset $\mathbf{d} \in \mathcal{D}$ (e.g., the 8 neighbors of a 3×3 stencil in 2D), and compute inflow by spatially shifting the outgoing flux fields using periodic boundary conditions.

Proposition 1 (Discrete Conservation). Under periodic boundary conditions, if every directed neighbor relation is symmetric (i.e., $j \in \mathcal{N}(i)$ implies $i \in \mathcal{N}(j)$), then the update above exactly preserves the global sum for each conserved channel: $\sum_i u_i^{t+1} = \sum_i u_i^t$.

The proof follows from observing that summing the update over all cells, $\sum_i \sum_j F_{i \rightarrow j}$ and $\sum_i \sum_j F_{j \rightarrow i}$ enumerate identical flux terms up to index renaming, hence cancel exactly. The full proof is provided in the appendix. This conservation property holds independently of how the fluxes F are produced, as long as the same transported amounts serve as outflow for the sender and inflow for the receiver.

3.3. Transport Heads

The central innovation is to produce fluxes corresponding to a feasible local transport plan rather than applying post-hoc corrections to predicted states. We adopt a backbone-head factorization: a convolutional ResNet-style encoder (He et al., 2016) with periodic padding maps inputs $[\mathbf{u}^t, \phi]$ to feature maps $\mathbf{z} = f_\theta([\mathbf{u}^t, \phi])$, and a transport head h_ψ via 1×1 convolution produces parameters for the chosen flux parameterization, which are then transformed via sigmoid, softmax, or softplus into physically interpretable quantities. This decoupling enables fair comparison between direct regression baselines using the same backbone and FluxNet variants differing only in head parameterization. Table 1 summarizes the transport head family.

For a stencil \mathcal{D} with $K = |\mathcal{D}|$ directions, the N-head sets the flux $F = \hat{F}$ directly as signed values, while the P-head sets $F = \text{softplus}(\hat{F})$ to ensure $F \geq 0$. Both preserve conservation via the update structure but neither enforces state bounds. In practice, P-head stabilizes training by eliminating flux sign oscillations, though it remains insufficient when strict physical bounds are required.

For fields satisfying a lower bound $u_i \geq \ell$, the L-head parameterizes capacity-limited outflow. Define the available amount $a_i = u_i - \ell$ that cell i can transfer without violating the lower bound. The head produces an outflow percentage $\alpha_i \in (0, 1)$ via sigmoid representing the fraction of available amount to transfer, and distribution weights $\pi_{i \rightarrow (i+\mathbf{d})} \geq 0$ with $\sum_{\mathbf{d} \in \mathcal{D}} \pi_{i \rightarrow (i+\mathbf{d})} = 1$ via softmax allocating outflow among neighbors. The outgoing flux is $F_{i \rightarrow (i+\mathbf{d})} = a_i \cdot \alpha_i \cdot \pi_{i \rightarrow (i+\mathbf{d})}$.

Proposition 2 (L-Head Lower Bound Guarantee). If $u_i^t \geq \ell$ for all i , then after one conservative transport update using L-head, $u_i^{t+1} \geq \ell$ for all i .

The proof follows from observing that the total outflow from cell i is $a_i \alpha_i < a_i = u_i - \ell$, so $u_i - \text{outflow} > \ell$, and since all inflow terms are nonnegative, the bound is preserved. This provides a hard structural guarantee without requiring post-hoc clipping.

For fields satisfying an upper bound $u_i \leq u_{\max}$, the U-head parameterizes capacity-limited inflow. Define the remaining capacity $b_i = u_{\max} - u_i$ that cell i can receive without violating the upper bound. The head produces an inflow percentage $\beta_i \in (0, 1)$ via sigmoid representing the fraction of remaining capacity to fill, and distribution weights $\rho_{j \rightarrow i} \geq 0$ with $\sum_{j \in \mathcal{N}(i)} \rho_{j \rightarrow i} = 1$ via softmax allocating how much to pull from each neighbor. The incoming flux is $F_{j \rightarrow i} = b_i \cdot \beta_i \cdot \rho_{j \rightarrow i}$.

Proposition 3 (U-Head Upper Bound Guarantee). If $u_i^t \leq u_{\max}$ for all i , then after one conservative transport update using U-head under periodic boundary conditions,

Table 1. Transport heads as feasible-set parameterizations.

| Head | Learned Object | Hard Constraint | Parameterization |
|------|-----------------------------------|--|--|
| N | Signed flux $F_{i \rightarrow j}$ | Conservation | Raw conv outputs |
| P | Positive outflow | Conservation | $\text{softplus}(\cdot)$ on flux |
| L | Capacity-limited outflow | Conserv. + $u \geq \ell$ | $\sigma(\cdot)$ outflow %, softmax dist. |
| U | Capacity-limited inflow | Conserv. + $u \leq u_{\max}$ | $\sigma(\cdot)$ inflow %, softmax dist. |
| D | Dual capacity (out/in) | Conservation (exact); dual-bound empirical via DCL | Two branches + DCL |

$$u_i^{t+1} \leq u_{\max} \text{ for all } i.$$

The proof follows from observing that the total inflow to cell i is $b_i \beta_i < b_i = u_{\max} - u_i$, so $u_i + \text{inflow} < u_{\max}$, and since all outflow terms are nonnegative, the bound is preserved. This provides a hard structural guarantee for upper bounds analogous to the L-head guarantee for lower bounds.

3.4. D-head

For doubly-bounded fields $u \in [\ell, u_{\max}]$, a single one-sided capacity constraint is insufficient. The D-head constructs two parallel transport plans: an outflow branch using available amount $a_i = u_i - \ell$ with L-head structure guaranteeing the sender cannot drop below ℓ , and an inflow branch using remaining capacity $b_i = u_{\max} - u_i$ with U-head structure guaranteeing the receiver cannot exceed u_{\max} . These two branches predict the same physical transport from opposite perspectives.

Each branch computes its own state change. The outflow branch computes the change from the outflow perspective: $\Delta u_i^{\text{out}} = -\sum_j F_{i \rightarrow j}^{\text{out}} + \sum_j F_{j \rightarrow i}^{\text{out}}$. The inflow branch computes the change from the inflow perspective: $\Delta u_i^{\text{in}} = -\sum_j F_{i \rightarrow j}^{\text{in}} + \sum_j F_{j \rightarrow i}^{\text{in}}$. The final state update averages these two change estimates:

$$u_i^{t+1} = u_i^t + \frac{1}{2} (\Delta u_i^{\text{out}} + \Delta u_i^{\text{in}}). \quad (3)$$

We enforce agreement between the two branches via the Dual Consistency Loss (DCL), which penalizes discrepancies in the predicted state changes:

$$\mathcal{L}_{\text{DCL}} = \frac{1}{|\Omega|} \sum_i |\Delta u_i^{\text{out}} - \Delta u_i^{\text{in}}|^2. \quad (4)$$

Each branch individually is conservative and satisfies a single-sided hard bound. However, the averaged update does not theoretically guarantee satisfaction of both bounds unless the two branches agree exactly. Therefore, in all dual-bounded experiments we report violation rates and conditional violation magnitudes as first-class metrics, rather than claiming strict two-sided feasibility. Empirically, DCL training drives violations to near-zero levels with negligible magnitudes.

3.5. FluxNet-LAP

The shallow water equations couple three conserved fields (h, m_x, m_y) where momentum transport depends strongly on mass transport. We introduce FluxNet-LAP, a task-specific instantiation that improves modeling fidelity without changing the core conservative update. Let h be water depth satisfying $h \geq 0$ and $\mathbf{m} = (m_x, m_y)$ be momentum fields. FluxNet-LAP predicts depth transport using an L-head, producing depth fluxes $F_{i \rightarrow j}^h$ with strict nonnegativity and $h \geq 0$ preservation. Momentum transport is decomposed into an advection term carried by mass transport, $F_{i \rightarrow j}^{m, \text{adv}} = F_{i \rightarrow j}^h \cdot \frac{m_i}{h_i + \varepsilon}$ where $\varepsilon > 0$ prevents division issues in near-dry regions, and a pressure term parameterized by a P-head with depth-squared gating, $F_{i \rightarrow j}^{m, \text{prs}} = h_i^2 \cdot \text{softplus}(\hat{G}_{i \rightarrow j})$. The total momentum flux is $F_{i \rightarrow j}^m = F_{i \rightarrow j}^{m, \text{adv}} + F_{i \rightarrow j}^{m, \text{prs}}$. The h^2 gating suppresses spurious momentum exchange in low-depth cells while permitting pressure-driven transport in wet regions. We emphasize that LAP is a shallow-water specialization; all other benchmarks use generic heads.

3.6. Training

All models are trained by minimizing prediction loss between surrogate rollouts and ground-truth trajectories. A common failure mode is exposure bias: training only on ground-truth inputs (teacher forcing) produces models that drift when consuming their own predictions at test time. We employ pushforward training (Brandstetter et al., 2022): during training, we unroll the model for K steps, feeding back its own predictions $\hat{\mathbf{u}}^{k+1} = \mathcal{T}_\theta(\hat{\mathbf{u}}^k, \phi)$ with $\hat{\mathbf{u}}^0 = \mathbf{u}^0$, and compute losses across the unrolled window:

$$\mathcal{L} = \sum_{k=1}^K \lambda_k \|\hat{\mathbf{u}}^k - \mathbf{u}^k\|_1 + \gamma \mathcal{L}_{\text{DCL}}, \quad (5)$$

where the DCL term applies when using the D-head. Push-forward training mitigates exposure bias, but if the predictor produces conservation drift or bound violations, errors still compound. The structural feasibility of FluxNet heads addresses precisely this coupling.

Table 2. Convection-diffusion rollout results at $T = 1$. Conservation error is near machine precision for all flux-based heads.

| Method | $\mathcal{E}_{\text{MAE}} (\times 10^{-3})$ | $\max \mathcal{E}_{\text{cons}}$ |
|------------------|---|----------------------------------|
| FluxNet-N | 4.49 ± 0.14 | 1.19×10^{-7} |
| FluxNet-P | 3.46 ± 0.10 | 2.38×10^{-7} |
| FluxNet-L | 1.82 ± 0.06 | 1.79×10^{-7} |

4. Experiments

We evaluate FluxNet on four representative conservative PDE benchmarks: 1D convection-diffusion (lower-bounded scalar), 2D shallow water equations (coupled depth-momentum with dry regions), 1D traffic flow (dual-bounded density with shocks), and 2D spinodal decomposition (dual-bounded phase field). All experiments use periodic boundary conditions. We compare against ResNet-AR with direct autoregressive regression using identical backbone capacity, FNO-AR with Fourier Neural Operator and residual prediction, soft conservation penalty methods (+SoftCons), post-hoc projection (+Box+Mass Projection) enforcing positivity followed by global mass renormalization, and output squashing (+SigmoidBound) for traffic flow. All autoregressive models use pushforward training with AdamW optimizer (Loshchilov & Hutter, 2017). We report rollout MAE at $T = 2 \times$ training horizon for temporal extrapolation, maximum conservation drift over the rollout, bound violation rate as percentage of spatiotemporal grid points violating bounds, and conditional violation magnitude as mean violation amplitude over violating points only. Additional experimental details including hyperparameters, dataset construction, and extended results are provided in the appendix.

4.1. Convection-Diffusion

The 1D convection-diffusion equation with lower-bounded concentration ($c \geq 0$) serves as a minimal benchmark to demonstrate the necessity of capacity-constrained heads. Table 2 reports rollout accuracy at $T = 1$. All flux-based heads maintain conservation at machine precision ($\sim 10^{-7}$). The L-head, which explicitly models lower-bound capacity, achieves the lowest MAE (1.82×10^{-3}), confirming that matching the head to physical constraints improves accuracy. Figure 5 in the appendix shows concentration profiles comparing the three variants, with L-head producing the smoothest evolution without spurious oscillations. FluxNet-N shows rollout oscillations due to unconstrained flux, while FluxNet-P is more stable; hence the N-head is not used in subsequent experiments.

4.2. Shallow Water Equations

The 2D shallow water equations couple three conserved fields: water depth h and momentum components (m_x, m_y).

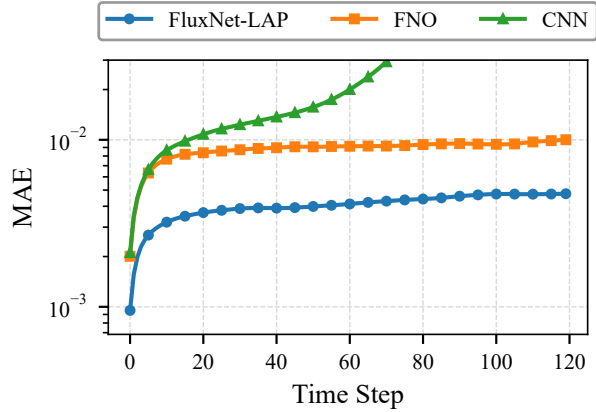


Figure 1. Rollout MAE over time for shallow water equations. Mean Absolute Error as a function of rollout time step for FluxNet-LAP, FNO, and CNN on the shallow water equation test set.

The key physical constraint is nonnegative depth ($h \geq 0$), and stable rollouts are challenging due to dry regions and strong mass-momentum coupling. Qualitative comparisons at the final rollout time ($T = 2$, corresponding to $2 \times$ temporal extrapolation) are provided in Figure 6 of the appendix. FluxNet-LAP closely matches ground truth across all three fields. Direct CNN regression exhibits severe high-frequency artifacts, while FNO shows localized distortions.

Figure 1 reports rollout MAE over time. FluxNet-LAP maintains the lowest error throughout the rollout horizon, while CNN-AR rapidly accumulates errors and becomes unstable. FNO-AR shows moderate error growth. Notably, projection-based methods achieve constraint satisfaction but at the cost of increased prediction error. Additional visualizations are provided in Figures 7–8 of the appendix.

Table 3 presents quantitative results at $T = 2$. FluxNet-LAP achieves the lowest MAE across all fields for both backbones, reducing depth MAE by 67% compared to the best projection baseline (3.12 vs. 6.74×10^{-3}). Conservation error reaches machine precision ($\sim 10^{-8}$), orders of magnitude lower than soft-constrained methods. Box+Mass projection achieves zero depth violations but incurs large momentum conservation errors due to nonlinear correction, while FluxNet-LAP satisfies all constraints structurally. Ablation studies examining the effect of different head combinations, pressure gating, and pushforward training are provided in Table 6 of the appendix.

4.3. Traffic Flow

The 1D Lighthill-Whitham-Richards (LWR) traffic model (Lighthill & Whitham, 1955; Richards, 1956) requires density $\rho \in [0, 1]$, providing an ideal testbed for dual-bounded transport. Test cases include shocks, rarefaction waves, and

Table 3. Shallow water equations: baseline comparison at $T = 2$ ($2 \times$ extrapolation). All methods use pushforward training. MAE values $\times 10^{-3}$. **Bold**: best in each backbone category.

| Method | $\mathcal{E}_{\text{MAE}} (\times 10^{-3})$ | | | $\mathcal{E}_{\text{cons}}$ | | | h Violation | |
|--------------------------|---|-----------------------------------|-----------------------------------|-----------------------------------|-----------------------------------|-----------------------------------|--------------------------------|---------------------------|
| | h | m_x | m_y | h | m_x | m_y | $\mathcal{V}_{\text{lb}} (\%)$ | \mathcal{M}_{lb} |
| <i>ResNet backbone</i> | | | | | | | | |
| ResNet-AR | 123 ± 4.2 | 88.4 ± 3.1 | 67.7 ± 2.4 | $4.0\text{e-}2$ | $4.2\text{e-}1$ | $2.7\text{e-}1$ | 5.18 | $2.2\text{e-}1$ |
| + SoftCons | 104 ± 3.5 | 115 ± 4.0 | 102 ± 3.6 | $1.7\text{e-}2$ | $9.3\text{e-}2$ | $5.9\text{e-}2$ | 6.82 | $4.2\text{e-}2$ |
| + Box+Mass Proj. | 22.1 ± 0.77 | 71.0 ± 2.5 | 49.4 ± 1.7 | $3.2\text{e-}7$ | $7.1\text{e-}1$ | $6.1\text{e-}1$ | 0.00 | – |
| FluxNet-LAP | 3.12 ± 0.11 | 4.41 ± 0.15 | 4.64 ± 0.16 | $3.3\text{e-}8$ | $6.0\text{e-}8$ | $3.2\text{e-}8$ | 0.00 | – |
| <i>FNO backbone</i> | | | | | | | | |
| FNO-AR | 7.26 ± 0.25 | 9.80 ± 0.34 | 9.40 ± 0.33 | $1.2\text{e-}2$ | $1.4\text{e-}1$ | $8.9\text{e-}2$ | 0.67 | $2.8\text{e-}3$ |
| + SoftCons | 15.9 ± 0.56 | 22.2 ± 0.78 | 22.0 ± 0.77 | $1.7\text{e-}3$ | $1.3\text{e-}2$ | $1.5\text{e-}2$ | 0.89 | $1.0\text{e-}2$ |
| + Box+Mass Proj. | 6.74 ± 0.24 | 12.9 ± 0.45 | 11.5 ± 0.40 | $3.3\text{e-}7$ | $3.6\text{e-}1$ | $2.4\text{e-}1$ | 0.00 | – |
| FluxNet-LAP (FNO) | 2.22 ± 0.08 | 3.26 ± 0.11 | 3.36 ± 0.12 | $3.3\text{e-}8$ | $5.7\text{e-}8$ | $3.4\text{e-}8$ | 0.00 | – |

complete flow blockages. Figure 2 shows density profiles at three time points. FluxNet-D accurately tracks shock formation and propagation while maintaining bounded predictions. FNO and CNN baselines exhibit visible overshoot near discontinuities.

Table 4 presents quantitative results. FluxNet-D achieves the best accuracy (MAE 3.48×10^{-3}) with machine-precision conservation. While SigmoidBound achieves zero violations, it catastrophically degrades accuracy (MAE 88.0 vs. 3.48). FluxNet-D exhibits small violation rates with negligible magnitudes ($< 10^{-3}$), demonstrating effective empirical dual-bound enforcement without sacrificing prediction quality. The D-head does not provide strict dual-bound guarantees, but the violations that do occur are low-amplitude excursions that do not destabilize the rollout. Ablation confirming the importance of DCL for balanced bound enforcement is provided in the appendix.

4.4. Spinodal Decomposition

The 2D Cahn-Hilliard equation (Cahn & Hilliard, 1958; Chen, 2002) models phase separation with a conserved, dual-bounded phase field $\phi \in [0, 1]$. This benchmark tests whether FluxNet-D remains a local transport operator at large time steps and whether it preserves statistical structure of microstructural evolution. We train three FluxNet-D models with temporal strides $10\Delta t$, $100\Delta t$, and $1000\Delta t$, enlarging the transport neighborhood radius proportionally to accommodate longer-range transport. All three stride models use the same training set: simulations from $t = 2000$ to $t = 52000\Delta t$, with snapshots saved every $10\Delta t$. Table 5 reports the multi-timestep model configurations and performance. The $1000\Delta t$ model achieves $17.3 \times$ speedup over GPU-accelerated explicit solvers while maintaining a localized effective receptive field (ERF) far smaller than its theoretical receptive field, confirming that FluxNet learns genuinely local transport operators even at large time steps.

The $100\Delta t$ model achieves the optimal accuracy-efficiency tradeoff with MAE of 2.16×10^{-2} .

Pointwise MAE does not capture whether surrogates preserve coarsening statistics. We evaluate the radial two-point correlation function $\bar{S}_2(r)$ (Torquato et al., 2002) computed via FFT-based autocorrelation. Figure 3 shows two-point statistics error evolution. As a baseline for inherent variability, we plot the correlation difference between two independent phase-field simulations with different random initial conditions. All three FluxNet-D models maintain errors comparable to this baseline throughout the extrapolation regime ($T = 1$ to $T = 2$), demonstrating that learned transport operators preserve microstructural coarsening statistics even beyond the training horizon.

To verify that FluxNet-D operates as a local transport operator, we perform gradient-based effective receptive field (ERF) analysis (Luo et al., 2016) on flux prediction channels. For each output channel corresponding to a specific neighbor direction, we compute the gradient of the channel output with respect to the input field, averaged over sampled locations from the test set. Figure 4 visualizes ERF patterns for the $10\Delta t$ model. Channels corresponding to specific neighbor directions show clear anisotropy aligned with their transport direction, while percentage channels are approximately isotropic. Despite increasing theoretical receptive field for larger strides, effective receptive fields remain substantially localized, supporting the physical interpretation of learned local transport.

5. Conclusion

We presented FluxNet, a family of neural PDE time-steppers that achieve structural conservation and bound preservation by learning capacity-constrained local transport operators. By shifting the prediction target from next-state values to feasible transport plans, FluxNet provides exact discrete con-

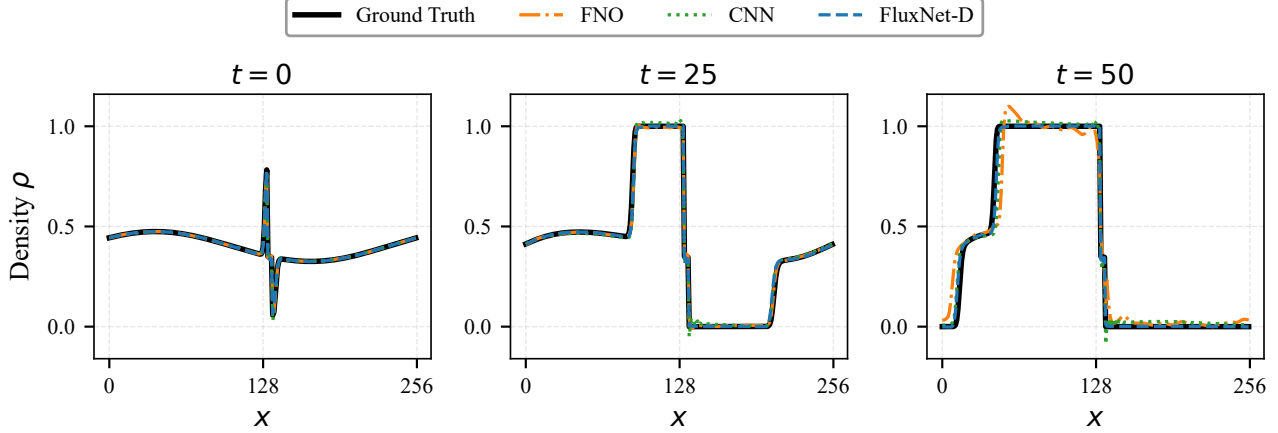


Figure 2. Traffic flow density profiles at selected time points. Comparison of density $\rho(x, t)$ predictions between ground truth, FluxNet-D, FNO, and CNN at three time points ($t = 0, t = 25, t = 50$).

Table 4. Traffic flow (LWR model): baseline comparison at $T = 2$. The density $\rho \in [0, 1]$ requires double-bound enforcement. MAE values $\times 10^{-3}$. **Bold**: best per backbone.

| Method | \mathcal{E}_{MAE} ($\times 10^{-3}$) | $\mathcal{E}_{\text{cons}}$ | \mathcal{V}_{lb} (%) | \mathcal{M}_{lb} ($\times 10^{-3}$) | \mathcal{V}_{ub} (%) | \mathcal{M}_{ub} ($\times 10^{-3}$) |
|---------------------------|--|-----------------------------|----------------------------------|---|----------------------------------|---|
| <i>ResNet backbone</i> | | | | | | |
| ResNet-AR | 15.9 ± 0.56 | 2.1e-2 | 0.32 | 37.6 | 3.20 | 15.6 |
| + SoftCons | 20.9 ± 0.73 | 1.6e-2 | 4.18 | 13.5 | 3.27 | 36.1 |
| + SigmoidBound + SoftCons | 88.0 ± 3.1 | 1.4e-1 | 0.00 | – | 0.00 | – |
| FluxNet-D | 3.48 ± 0.12 | 7.7e-8 | 0.52 | 1.13 | 2.87 | 0.84 |
| <i>FNO backbone</i> | | | | | | |
| FNO-AR | 6.85 ± 0.24 | 5.8e-3 | 1.95 | 4.76 | 1.88 | 7.37 |
| + SoftCons | 8.83 ± 0.31 | 2.7e-3 | 3.22 | 6.88 | 1.11 | 12.1 |
| FluxNet-D (FNO) | 4.01 ± 0.14 | 7.4e-8 | 7.09 | 2.50 | 2.01 | 3.55 |

Table 5. Spinodal decomposition: multi-timestep FluxNet-D models. r : transport neighborhood radius; RF: theoretical receptive field; ERF: effective receptive field. Results at $T = 2$.

| Δt_{model} | r | RF _{theo} | ERF | Speedup | MAE ($\times 10^{-2}$) |
|---------------------------|-----|--------------------|----------|---------------|-----------------------------------|
| $10\Delta t$ | 3 | 19^2 | 9.7^2 | 0.55 \times | 2.76 ± 0.10 |
| $100\Delta t$ | 5 | 37^2 | 12.2^2 | 3.8 \times | 2.16 ± 0.08 |
| $1000\Delta t$ | 9 | 79^2 | 19.0^2 | 17.3 \times | 8.39 ± 0.29 |

servation under periodic boundaries with drift at machine precision, hard lower-bound guarantees via capacity-limited outflow through the L-head, effective dual-bound control via dual consistency regularization through the D-head with transparent violation reporting, and large-timestep capability through configurable stencil radii enabling significant computational speedups. Across four diverse benchmarks spanning different physics and constraint types, FluxNet consistently outperforms direct regression baselines and soft-constraint methods in long-rollout accuracy while satisfying physical constraints. The learned transport operators

preserve not only pointwise accuracy but also statistical properties of microstructural evolution, as demonstrated through two-point correlation analysis on spinodal decomposition.

Several limitations warrant future investigation. Our theoretical guarantees hold for periodic boundaries, and extending to Dirichlet, Neumann, or mixed boundary conditions requires careful treatment of boundary fluxes. We consider source-free conservation laws, and incorporating source terms while maintaining conservation requires additional validation. The D-head provides strong empirical bound satisfaction but not strict theoretical guarantees, and future work could explore hybrid approaches combining transport heads with lightweight projection layers. The fixed neighborhood size is a hyperparameter that must be tuned for each timestep, and adaptive or multi-scale neighborhoods could improve flexibility. Extension to unstructured meshes, potentially by combining with graph neural network architectures, would broaden the scope of applicability. Despite these limitations, FluxNet demonstrates that structural in-

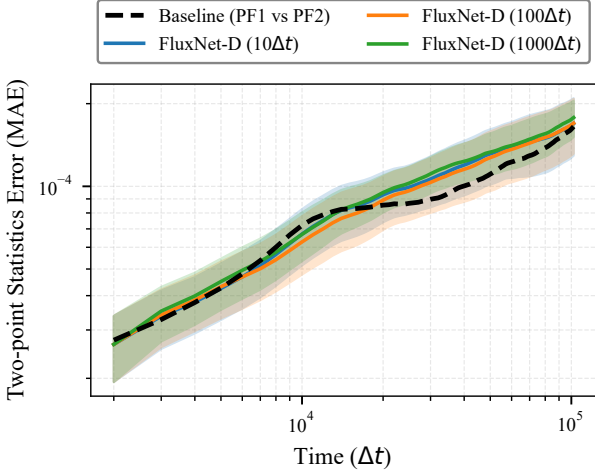


Figure 3. Two-point statistics error evolution for spinodal decomposition. MAE of the radial two-point correlation function as a function of simulation time for FluxNet-D models trained with different time step sizes. Shaded regions indicate ± 1 standard deviation over 100 independent rollouts. The baseline error between two independent phase-field simulations is shown for reference.

corporation of physical constraints into neural architecture design yields substantial benefits for stable, accurate, and physically meaningful long-horizon predictions.

Impact Statement

This paper presents work whose goal is to advance the field of scientific machine learning by introducing physically rigorous neural surrogates. The primary impact of FluxNet lies in its ability to accelerate complex PDE simulations by orders of magnitude without sacrificing physical validity, potentially reducing the massive computational energy footprint associated with large-scale scientific modeling in climate science and engineering. By structurally enforcing conservation laws and bounds, our method mitigates the risk of unphysical predictions that typically plague data-driven solvers, thereby enhancing the reliability of AI-driven systems in safety-critical applications. There are no specific negative societal consequences or dual-use risks that we feel must be highlighted here.

References

Battaglia, P. W., Hamrick, J. B., Bapst, V., Sanchez-Gonzalez, A., Zambaldi, V., Malinowski, M., Tacchetti, A., Raposo, D., Santoro, A., Faulkner, R., et al. Relational inductive biases, deep learning, and graph networks. *arXiv preprint arXiv:1806.01261*, 2018.

Bengio, S., Vinyals, O., Jaitly, N., and Shazeer, N. Scheduled sampling for sequence prediction with recurrent neu-

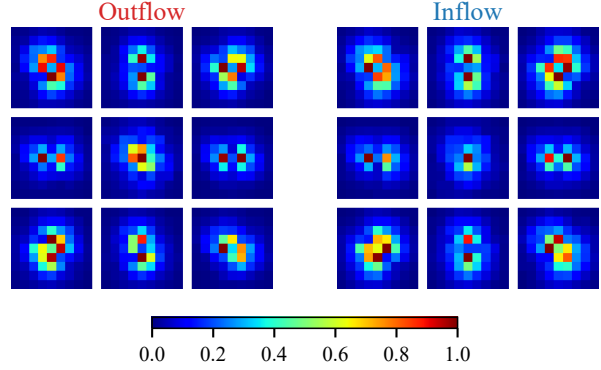


Figure 4. Effective receptive field analysis for FluxNet-D (10 Δt). Visualization of the ERF for each output channel. The localized and anisotropic patterns confirm that the learned flux operators depend only on local neighborhood information.

ral networks. *Advances in Neural Information Processing Systems*, 28, 2015.

Brandstetter, J., Worrall, D., and Welling, M. Message passing neural PDE solvers. *arXiv preprint arXiv:2202.03376*, 2022.

Cahn, J. W. and Hilliard, J. E. Free energy of a nonuniform system. I. interfacial free energy. *The Journal of Chemical Physics*, 28(2):258–267, 1958.

Chen, L.-Q. Phase-field models for microstructure evolution. *Annual Review of Materials Research*, 32(1):113–140, 2002.

Gilmer, J., Schoenholz, S. S., Riley, P. F., Vinyals, O., and Dahl, G. E. Neural message passing for quantum chemistry. In *Proceedings of the International Conference on Machine Learning*, pp. 1263–1272. PMLR, 2017.

Gupta, J. K. and Brandstetter, J. Towards multi-spatiotemporal-scale generalized PDE modeling. *arXiv preprint arXiv:2209.15616*, 2022.

He, K., Zhang, X., Ren, S., and Sun, J. Deep residual learning for image recognition. In *Proceedings of the IEEE Conference on Computer Vision and Pattern Recognition*, pp. 770–778, 2016.

Horie, M. and Mitsume, N. Physics-embedded neural networks: Graph neural PDE solvers with mixed boundary conditions. *Advances in Neural Information Processing Systems*, 35:23218–23229, 2022.

Karlbauer, M., Praditia, T., Otte, S., Oladyshkin, S., Nowak, W., and Butz, M. V. Composing partial differential equations with physics-aware neural networks. In *Proceedings of the International Conference on Machine Learning*, pp. 10773–10801. PMLR, 2022.

Kochkov, D., Smith, J. A., Alieva, A., Wang, Q., Brenner, M. P., and Hoyer, S. Machine learning–accelerated computational fluid dynamics. *Proceedings of the National Academy of Sciences*, 118(21):e2101784118, 2021.

LeVeque, R. J. *Finite Volume Methods for Hyperbolic Problems*, volume 31. Cambridge University Press, 2002.

Li, Z., Kovachki, N., Azizzadenesheli, K., Liu, B., Bhattacharya, K., Stuart, A., and Anandkumar, A. Fourier neural operator for parametric partial differential equations. *arXiv preprint arXiv:2010.08895*, 2020.

Li, Z., Liu-Schiavini, M., Kovachki, N., Azizzadenesheli, K., Liu, B., Bhattacharya, K., Stuart, A., and Anandkumar, A. Learning chaotic dynamics in dissipative systems. *Advances in Neural Information Processing Systems*, 35: 16768–16781, 2022.

Lighthill, M. J. and Whitham, G. B. On kinematic waves II: a theory of traffic flow on long crowded roads. *Proceedings of the Royal Society of London. Series A. Mathematical and Physical Sciences*, 229(1178):317–345, 1955.

Lippe, P., Veeling, B., Perdikaris, P., Turner, R., and Brandstetter, J. PDE-refiner: Achieving accurate long rollouts with neural PDE solvers. *Advances in Neural Information Processing Systems*, 36:67398–67433, 2023.

Liu, L., Zhang, L., and Gelb, A. Neural entropy-stable conservative flux form neural networks for learning hyperbolic conservation laws. *arXiv preprint arXiv:2507.01795*, 2025.

Loshchilov, I. and Hutter, F. Decoupled weight decay regularization. *arXiv preprint arXiv:1711.05101*, 2017.

Luo, W., Li, Y., Urtasun, R., and Zemel, R. Understanding the effective receptive field in deep convolutional neural networks. *Advances in Neural Information Processing Systems*, 29, 2016.

Matsubara, T., Ishikawa, A., and Yaguchi, T. Deep energy-based modeling of discrete-time physics. *Advances in Neural Information Processing Systems*, 33:13100–13111, 2020.

Pfaff, T., Fortunato, M., Sanchez-Gonzalez, A., and Battaglia, P. Learning mesh-based simulation with graph networks. In *Proceedings of the International Conference on Learning Representations*, 2020.

Praditia, T., Karlbauer, M., Otte, S., Oladyshkin, S., Butz, M. V., and Nowak, W. Finite volume neural network: Modeling subsurface contaminant transport. *arXiv preprint arXiv:2104.06010*, 2021.

Raissi, M., Perdikaris, P., and Karniadakis, G. E. Physics-informed neural networks: A deep learning framework for solving forward and inverse problems involving nonlinear partial differential equations. *Journal of Computational Physics*, 378:686–707, 2019.

Richards, P. I. Shock waves on the highway. *Operations Research*, 4(1):42–51, 1956.

Ross, S., Gordon, G., and Bagnell, D. A reduction of imitation learning and structured prediction to no-regret online learning. In *Proceedings of the Fourteenth International Conference on Artificial Intelligence and Statistics*, pp. 627–635. JMLR Workshop and Conference Proceedings, 2011.

Sanchez-Gonzalez, A., Godwin, J., Pfaff, T., Ying, R., Leskovec, J., and Battaglia, P. Learning to simulate complex physics with graph networks. In *Proceedings of the International Conference on Machine Learning*, pp. 8459–8468. PMLR, 2020.

Singha, M. Learning under laws: A constraint-projected neural PDE solver that eliminates hallucinations. *arXiv preprint arXiv:2511.03578*, 2025.

Timm, K., Kusumaatmaja, H., Kuzmin, A., Shadrt, O., Silva, G., and Viggen, E. The lattice Boltzmann method: Principles and practice. *Cham, Switzerland: Springer International Publishing AG*, 2016.

Torquato, S. et al. *Random Heterogeneous Materials: Microstructure and Macroscopic Properties*, volume 16. Springer, 2002.

Van Leer, B. Towards the ultimate conservative difference scheme. V. a second-order sequel to Godunov’s method. *Journal of Computational Physics*, 32(1):101–136, 1979.

Wang, S., Wang, H., and Perdikaris, P. Learning the solution operator of parametric partial differential equations with physics-informed DeepONets. *Science Advances*, 7(40): eabi8605, 2021.

Zhang, X. and Shu, C.-W. On positivity-preserving high order discontinuous Galerkin schemes for compressible Euler equations on rectangular meshes. *Journal of Computational Physics*, 229(23):8918–8934, 2010.

A. Theoretical Properties and Proofs

This section provides complete proofs for the theoretical propositions stated in the main text, along with a detailed discussion of the guarantees and limitations of the D-head for dual-bounded transport.

Proposition 1 (Discrete Conservation). Consider a regular grid $\Omega = \{1, 2, \dots, N\}^d$ with periodic boundary conditions. Let $\mathcal{N}(i)$ denote the neighborhood of cell i such that $j \in \mathcal{N}(i) \Leftrightarrow i \in \mathcal{N}(j)$ (symmetric stencil). For any flux field $\{F_{i \rightarrow j}\}_{i,j}$, the transport update

$$u_i^{t+1} = u_i^t - \sum_{j \in \mathcal{N}(i)} F_{i \rightarrow j} + \sum_{j \in \mathcal{N}(i)} F_{j \rightarrow i} \quad (6)$$

exactly preserves the global sum: $\sum_{i \in \Omega} u_i^{t+1} = \sum_{i \in \Omega} u_i^t$.

Proof. Summing the update equation over all cells in the domain yields:

$$\sum_{i \in \Omega} u_i^{t+1} = \sum_{i \in \Omega} u_i^t - \sum_{i \in \Omega} \sum_{j \in \mathcal{N}(i)} F_{i \rightarrow j} + \sum_{i \in \Omega} \sum_{j \in \mathcal{N}(i)} F_{j \rightarrow i}. \quad (7)$$

Consider the outflow term $S_{\text{out}} = \sum_{i \in \Omega} \sum_{j \in \mathcal{N}(i)} F_{i \rightarrow j}$. Each directed pair (i, j) with $j \in \mathcal{N}(i)$ contributes $F_{i \rightarrow j}$ exactly once to this sum. Similarly, consider the inflow term $S_{\text{in}} = \sum_{i \in \Omega} \sum_{j \in \mathcal{N}(i)} F_{j \rightarrow i}$. By the symmetry condition $j \in \mathcal{N}(i) \Leftrightarrow i \in \mathcal{N}(j)$, we can relabel the summation indices. Setting $i' = j$ and $j' = i$, we obtain:

$$S_{\text{in}} = \sum_{i \in \Omega} \sum_{j \in \mathcal{N}(i)} F_{j \rightarrow i} = \sum_{j' \in \Omega} \sum_{i' \in \mathcal{N}(j')} F_{i' \rightarrow j'} = \sum_{i \in \Omega} \sum_{j \in \mathcal{N}(i)} F_{i \rightarrow j} = S_{\text{out}}. \quad (8)$$

The key insight is that the symmetric neighborhood relation under periodic boundaries ensures that the set of all directed pairs (i, j) with $j \in \mathcal{N}(i)$ is identical when enumerated from either endpoint. Therefore, the outflow and inflow sums are equal, and they cancel in the global sum:

$$\sum_{i \in \Omega} u_i^{t+1} = \sum_{i \in \Omega} u_i^t - S_{\text{out}} + S_{\text{in}} = \sum_{i \in \Omega} u_i^t. \quad (9)$$

This completes the proof.

This proof holds for any flux values, including signed fluxes (N-head), non-negative fluxes (P-head), or capacity-constrained fluxes (L/U/D-heads). Conservation is a structural property of the update rule itself, independent of how the fluxes are computed by the neural network.

Proposition 2 (L-Head Lower Bound Guarantee). Let ℓ be a lower bound. Suppose $u_i^t \geq \ell$ for all $i \in \Omega$. Define the available amount $a_i = u_i^t - \ell \geq 0$. The L-head parameterizes an outflow percentage $\alpha_i = \sigma(z_i) \in (0, 1)$ where σ is the sigmoid function, and a distribution $\pi_{i \rightarrow j} = \text{softmax}_j(w_{ij}) \geq 0$ with $\sum_{j \in \mathcal{N}(i)} \pi_{i \rightarrow j} = 1$. The outgoing flux is $F_{i \rightarrow j} = a_i \cdot \alpha_i \cdot \pi_{i \rightarrow j}$. Then after one transport update, $u_i^{t+1} > \ell$ for all i .

Proof. The total outflow from cell i is computed as:

$$\text{Outflow}_i = \sum_{j \in \mathcal{N}(i)} F_{i \rightarrow j} = a_i \alpha_i \sum_{j \in \mathcal{N}(i)} \pi_{i \rightarrow j} = a_i \alpha_i. \quad (10)$$

The last equality follows from the softmax normalization constraint $\sum_j \pi_{i \rightarrow j} = 1$. Since $\alpha_i \in (0, 1)$ (the sigmoid function never saturates to exactly 0 or 1 for finite inputs), we have the strict inequality:

$$\text{Outflow}_i = a_i \alpha_i < a_i = u_i^t - \ell. \quad (11)$$

The total inflow to cell i from its neighbors is:

$$\text{Inflow}_i = \sum_{j \in \mathcal{N}(i)} F_{j \rightarrow i} = \sum_{j \in \mathcal{N}(i)} a_j \alpha_j \pi_{j \rightarrow i} \geq 0, \quad (12)$$

where non-negativity follows from $a_j \geq 0$, $\alpha_j > 0$, and $\pi_{j \rightarrow i} \geq 0$. Combining these results:

$$u_i^{t+1} = u_i^t - \text{Outflow}_i + \text{Inflow}_i > u_i^t - (u_i^t - \ell) + 0 = \ell. \quad (13)$$

This completes the proof.

The strict inequality $u_i^{t+1} > \ell$ (rather than \geq) arises because sigmoid outputs lie in the open interval $(0, 1)$. This provides a small numerical buffer above the bound, which is beneficial for stability in practice.

D-Head: Guarantees and Limitations. The D-head is designed for fields with dual bounds $u \in [\ell, u_{\max}]$, where a single one-sided capacity constraint is insufficient. The D-head constructs two parallel transport plans from complementary perspectives.

The outflow branch computes $F_{i \rightarrow j}^{\text{out}}$ using the available amount $a_i = u_i - \ell$ following the L-head structure. By the same argument as Proposition 2, if the state update were performed using only the outflow branch fluxes, then $u_i^{t+1, \text{out}} > \ell$ would be guaranteed.

The inflow branch computes $F_{i \rightarrow j}^{\text{in}}$ using the remaining capacity $b_j = u_{\max} - u_j$ following the U-head structure. The inflow percentage $\beta_j = \sigma(z_j) \in (0, 1)$ and distribution $\rho_{i \rightarrow j} = \text{softmax}_i(w_{ij}) \geq 0$ determine how much each receiver cell pulls from its neighbors. By an analogous argument, if the state update were performed using only the inflow branch fluxes, then $u_j^{t+1, \text{in}} < u_{\max}$ would be guaranteed.

Each branch individually is conservative (by Proposition 1) and satisfies a single-sided hard bound. However, the final transported amount is computed as their average: $F_{i \rightarrow j} = \frac{1}{2}(F_{i \rightarrow j}^{\text{out}} + F_{i \rightarrow j}^{\text{in}})$. This averaged flux does not inherit strict guarantees for both bounds unless $F^{\text{out}} = F^{\text{in}}$. Consider a scenario where $F_{i \rightarrow j}^{\text{out}}$ is large (the sender has ample available amount) but $F_{i \rightarrow j}^{\text{in}}$ is small (the receiver has limited capacity). The average may exceed what the receiver can safely absorb, leading to a potential upper-bound violation.

The Dual Consistency Loss (DCL) encourages agreement between the two branches during training (see Eq. (4) in the main text). When the two branches agree closely, the averaged update inherits the feasibility properties of both. In all experiments, we observe that DCL training drives violation rates below 3% with conditional violation magnitudes of $O(10^{-3})$, far smaller than unconstrained baselines. We report these violation statistics transparently as first-class metrics rather than claiming strict theoretical guarantees for dual-bounded enforcement.

B. Convection-Diffusion

The 1D convection-diffusion equation serves as a minimal benchmark to validate the flux-based parameterization and demonstrate the benefit of matching the transport head to the physical constraint structure.

The governing equation describes the transport and diffusion of a conserved concentration field $c(x, t) \geq 0$:

$$\frac{\partial c}{\partial t} + u \frac{\partial c}{\partial x} = D \frac{\partial^2 c}{\partial x^2}, \quad (t, x) \in (0, T] \times [0, L], \quad (14)$$

with periodic boundary conditions $c(t, 0) = c(t, L)$. The advection velocity u governs the transport rate while the diffusion coefficient D controls the smoothing rate. Total mass $\int_0^L c \, dx$ is conserved, and physical concentrations must remain non-negative.

The dataset is constructed as follows. We set domain length $L = 1.0$ and diffusion coefficient $D = 0.005$. For each trajectory, the advection velocity is sampled uniformly as $u \sim \mathcal{U}(0.0, 0.2)$. Initial conditions are generated as superpositions of four sinusoidal modes with random phases, with amplitudes scaled to ensure $c_0(x) \in [0, 1]$. The spatial domain is discretized on a grid of $N = 32$ points (downsampled from 64 for efficiency). The solver employs a Fourier spectral method with an exact integrating factor for temporal integration, ensuring high numerical accuracy. We simulate $T_{\max} = 5.0$ time units, saving snapshots every $\Delta t_{\text{save}} = 0.1$, yielding 51 frames per trajectory. The dataset split consists of 100 training, 10 validation, and 10 test trajectories.

All FluxNet models for this benchmark use a ResNet backbone with 32 base channels, 4 residual blocks, and kernel size 3. The transport neighborhood is a 3-point stencil (left and right neighbors). Training employs the AdamW optimizer with learning rate 10^{-3} , weight decay 10^{-2} , and 100 epochs with cosine learning rate decay. Since this benchmark focuses on validating the head design rather than long-horizon stability, we use one-step training (no pushforward unrolling).

Figure 5 compares concentration profiles predicted by the three FluxNet variants (N-head, P-head, L-head) against ground truth at five representative time points spanning the rollout. At early rollout stages, all three variants exhibit exceptional agreement with the ground truth. As the rollout advances, however, their behaviors diverge: the L-head preserves the highest

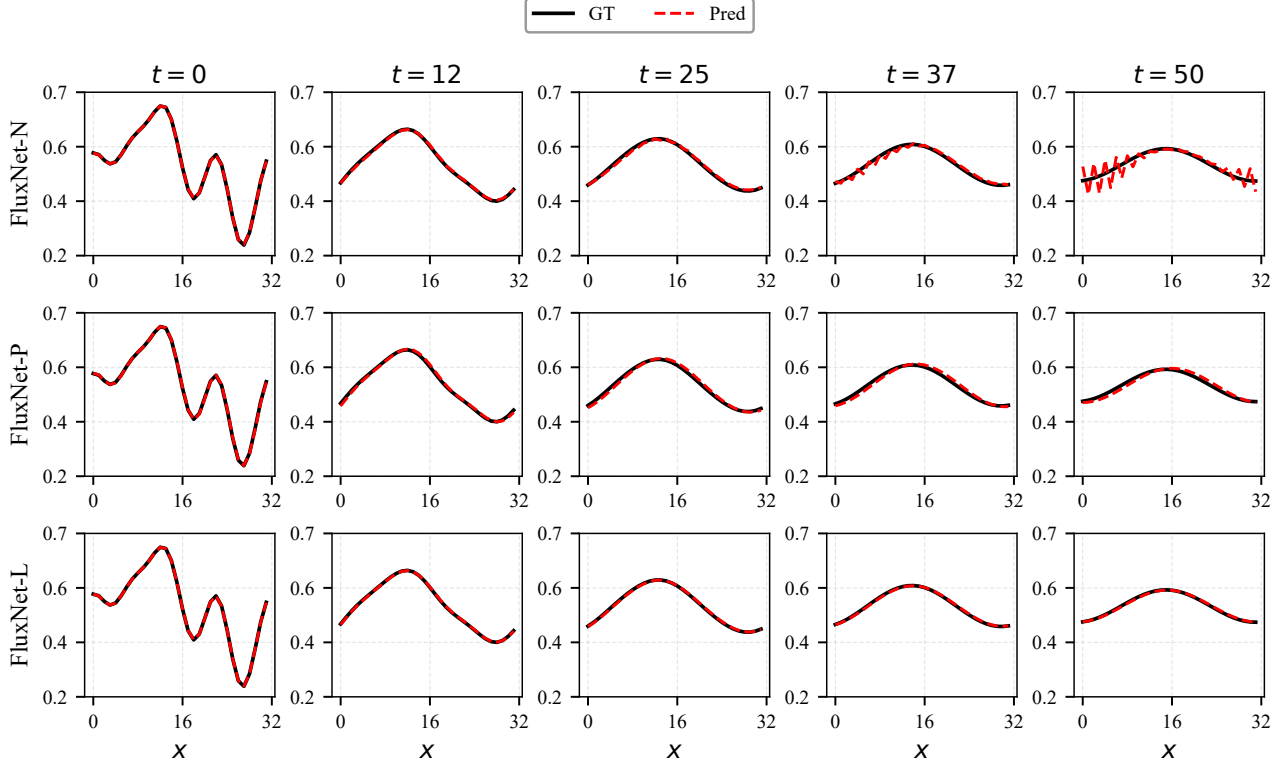


Figure 5. Concentration profiles at five time points comparing FluxNet-N (unconstrained), FluxNet-P (positive flux), and FluxNet-L (lower-bounded) variants on the 1D convection-diffusion equation. All three variants maintain good agreement with ground truth in smooth regions. The L-head produces the most accurate tracking near concentration minima approaching zero.

accuracy with virtually no deviation, the P-head shows minor drift while remaining stable, whereas the N-head develops oscillations in later stages. These observations align with the quantitative results in Table 2 of the main text, where the L-head achieves the lowest MAE (1.82 vs. 3.46 for P-head and 4.49 for N-head) while all variants maintain conservation error at machine precision. The improved accuracy of the L-head arises because its capacity-limited outflow naturally respects the non-negativity constraint, avoiding numerical artifacts from signed flux cancellations near zero concentration.

C. Shallow Water

The 2D shallow water equations provide a challenging benchmark for coupled multi-field conservation with a strict positivity constraint on water depth.

The governing equations couple three conserved fields: water depth $h \geq 0$ and momentum components $(m_x, m_y) = h(u, v)$ where (u, v) is the velocity field:

$$\frac{\partial h}{\partial t} + \nabla \cdot (h\mathbf{v}) = 0, \quad (15)$$

$$\frac{\partial \mathbf{m}}{\partial t} + \nabla \cdot (\mathbf{m} \otimes \mathbf{v}) = -gh\nabla h, \quad (16)$$

where $g = 9.81 \text{ m/s}^2$ is gravitational acceleration. The physical constraint $h \geq 0$ is strict; negative water depths are physically meaningless and cause numerical instabilities through the velocity computation $\mathbf{v} = \mathbf{m}/h$.

The dataset is constructed on a doubly-periodic domain $[0, 10]^2$ discretized on a 64×64 grid (downsampled from 128×128). The numerical solver employs a finite volume method with Rusanov flux and SSP-RK3 time stepping at $\Delta t = 0.004$. Initial conditions span four categories designed to test different physical regimes: Case A1 uses Gaussian superposition with zero initial momentum and 5-35% dry region coverage; Case A2 employs Fourier synthesis for smoother initial depth profiles,

Table 6. Shallow water equations: ablation study at $T = 2$. PPP: P-head for all fields; LPP: L-head for h , P-head for momentum; PAP: P-head for h with advection-pressure momentum decomposition. All MAE values are $\times 10^{-3}$.

| Variant | $\mathcal{E}_{\text{MAE}} (\times 10^{-3})$ | | | $\mathcal{E}_{\text{cons}}$ | | | h Violation $\mathcal{V}_{\text{lb}} (\%)$ |
|---------------------------|---|-----------------------------------|-----------------------------------|-----------------------------|----------------------------|----------------------------|---|
| | h | m_x | m_y | h | m_x | m_y | |
| FluxNet-PPP | 191 ± 6.7 | 120 ± 4.2 | 64.8 ± 2.3 | $1.88e-7$ | $9.9e-7$ | $1.2e-6$ | 7.92 |
| FluxNet-LPP | 7.91 ± 0.28 | 16.6 ± 0.58 | 22.4 ± 0.78 | $3.10e-8$ | $1.2e-6$ | $9.6e-7$ | 0.00 |
| FluxNet-PAP | | | | Diverged | | | |
| LAP (w/o pressure gating) | 8.96 ± 0.31 | 10.3 ± 0.36 | 10.0 ± 0.35 | $3.38e-8$ | $1.2e-6$ | $1.0e-6$ | 0.00 |
| LAP (w/o pushforward) | 2.84 ± 0.10 | 3.90 ± 0.14 | 4.22 ± 0.15 | $3.32e-8$ | $5.9e-8$ | $4.1e-8$ | 0.00 |
| FluxNet-LAP | 3.12 ± 0.11 | 4.41 ± 0.15 | 4.64 ± 0.16 | $3.31e-8$ | $6.0e-8$ | $3.2e-8$ | 0.00 |

also with zero momentum; Case B1 and B2 extend A1 and A2 respectively with non-zero initial momentum fields to test coupled dynamics. The training horizon is $T_{\text{train}} = 2.4$, and test rollouts extend to $T_{\text{test}} = 4.8$, representing $2\times$ temporal extrapolation. The dataset split consists of 50 training, 20 validation, and 50 test trajectories, stratified across the four case types.

FluxNet-LAP uses a ResNet backbone with 64 base channels, 4 residual blocks, and kernel size 3. The transport neighborhood is a 3×3 stencil (8 neighbors). Training employs pushforward unrolling with a fixed unroll length of 5 steps over 100 epochs.

Table 6 presents the ablation study results. Enforcing $h \geq 0$ via the L-head is essential: the PPP variant (P-head for all fields) exhibits a 7.92% depth violation rate and approximately 60 \times higher MAE than the full LAP model. The LPP variant (L-head for depth, P-head for momentum without advection-pressure decomposition) achieves zero depth violations but shows higher momentum error than LAP, indicating that the advection-pressure decomposition improves momentum flux learning. The PAP variant (P-head for depth with advection-pressure coupling for momentum) diverges during training because the momentum advection term $F_{i \rightarrow j}^{m,\text{adv}} = F_{i \rightarrow j}^h \cdot m_i / (h_i + \varepsilon)$ becomes unstable when the P-head permits small negative depth predictions. Removing the h^2 pressure gating increases momentum error by approximately 2 \times , confirming that the gating improves robustness near dry regions where spurious momentum exchange should be suppressed. Interestingly, the variant without pushforward training achieves similar or slightly better MAE than the full model, suggesting that the strong structural constraints from conservation and bound preservation already mitigate much of the exposure bias that pushforward training is designed to address.

Figures 6, 7, and 8 show the time evolution of the three conserved fields (h, m_x, m_y) comparing ground truth against FluxNet-LAP, FNO, and CNN predictions at six time steps spanning the rollout. FluxNet-LAP maintains accurate field evolution throughout the rollout horizon, closely tracking the ground truth wetting-drying fronts and momentum transport patterns. The CNN baseline develops severe checkerboard artifacts by mid-trajectory, particularly visible in the momentum fields, indicating instability in the learned dynamics. FNO exhibits localized distortions near wave fronts and wetting-drying boundaries, though it maintains better global structure than CNN. These qualitative observations are consistent with the quantitative results in Table 3 of the main text, where FluxNet-LAP achieves an order of magnitude lower MAE than baselines.

D. Traffic Flow

The 1D traffic flow problem based on the Lighthill-Whitham-Richards (LWR) model provides an ideal testbed for dual-bounded transport, as the density must satisfy $\rho \in [0, 1]$ and the dynamics feature shocks and rarefaction waves that challenge bound preservation.

The governing equation is a scalar conservation law with a nonlinear flux function:

$$\frac{\partial \rho}{\partial t} + \frac{\partial}{\partial x} [v_{\max}(x)\rho(1 - \rho)] = 0, \quad (17)$$

where $\rho \in [0, 1]$ represents the normalized traffic density (fraction of road capacity), and $v_{\max}(x)$ is the spatially-varying maximum velocity. The flux function $Q(\rho) = v_{\max}\rho(1 - \rho)$ is concave with maximum at $\rho = 0.5$, leading to characteristic shock formation when high-density regions encounter low-density regions.

Table 7. Traffic flow: ablation study at $T = 2$. P/L/U: single-constraint heads. The D-head with DCL achieves the best trade-off between accuracy and balanced bound enforcement.

| Variant | \mathcal{E}_{MAE} ($\times 10^{-3}$) | $\mathcal{E}_{\text{cons}}$ ($\times 10^{-7}$) | \mathcal{V}_{lb} (%) | \mathcal{M}_{lb} ($\times 10^{-3}$) | \mathcal{V}_{ub} (%) | \mathcal{M}_{ub} ($\times 10^{-3}$) |
|---------------------|--|---|----------------------------------|---|----------------------------------|---|
| FluxNet-P | 6.82 ± 0.24 | 6.17 | 1.37 | 8.00 | 0.26 | 11.3 |
| FluxNet-L | 4.80 ± 0.17 | 1.04 | 0.00 | — | 1.10 | 4.60 |
| FluxNet-U | 5.05 ± 0.18 | 1.25 | 6.68 | 9.78 | 0.00 | — |
| D (w/o DCL) | 3.49 ± 0.12 | 0.784 | 2.41 | 1.99 | 2.88 | 2.96 |
| D (w/o pushforward) | 8.09 ± 0.28 | 0.845 | 0.50 | 1.16 | 0.00 | — |
| FluxNet-D | 3.48 ± 0.12 | 0.771 | 0.52 | 1.13 | 1.87 | 0.838 |

The dataset is constructed on a periodic domain $[0, 10]$ (representing a ring road) discretized on $N = 256$ grid points. The numerical solver uses a first-order finite volume method with Rusanov flux at $\Delta t = 0.016$. Initial conditions span seven case types designed to probe different physical regimes: Case 1 (traffic jam) features a ramp-plateau profile creating shock-rarefaction interactions; Case 2A (speed limit zone) has smooth spatial variation in v_{max} ; Case 2B (red light) models complete flow blockage; Cases 3+, 3-, and 3₀ are Riemann problems with forward, backward, and stationary shocks respectively; Case 4 generates rarefaction waves. The training horizon is $T_{\text{train}} = 4.0$, and test rollouts extend to $T_{\text{test}} = 8.0$ ($2 \times$ extrapolation). The dataset split consists of 100 training, 50 validation, and 100 test trajectories.

FluxNet-D uses a ResNet backbone with 32 base channels, 6 residual blocks, and kernel size 5. The transport neighborhood is a 11-point stencil. Training employs pushforward unrolling over 100 epochs with DCL weight $\gamma = 0.1$.

Table 7 presents the ablation study results for the traffic flow benchmark. Single-sided heads strictly enforce their respective bounds but violate the opposite: the L-head achieves zero lower-bound violations but 1.10% upper-bound violations, while the U-head shows the reverse pattern with 6.68% lower-bound violations but zero upper-bound violations. The P-head, which only enforces non-negative fluxes without capacity constraints, exhibits violations on both sides. Removing the DCL from the D-head increases violation rates by approximately $4 \times$ on both bounds (from 0.52% to 2.41% for lower bound, from 1.87% to 2.88% for upper bound), confirming that dual consistency regularization is essential for balanced enforcement. The conditional violation magnitudes remain small in all D-head variants, but DCL training reduces them further. Notably, pushforward training is critical for this shock-dominated benchmark: removing it increases MAE from 3.48 to 8.09 ($\times 10^{-3}$), a $2.3 \times$ degradation. This sensitivity arises because shock dynamics are inherently sensitive to distributional shift; errors in shock position or speed compound rapidly during rollout.

E. Spinodal Decomposition

The 2D Cahn-Hilliard equation models spinodal decomposition with a conserved phase field $\phi \in [0, 1]$. This benchmark tests whether FluxNet-D remains a genuinely local transport operator when trained for large time steps, and whether it preserves the statistical structure of microstructural evolution beyond pointwise error metrics.

The governing equation is a fourth-order parabolic PDE describing phase separation dynamics:

$$\frac{\partial c}{\partial t} = M \nabla^2 \mu, \quad \mu = f'(c) - \kappa \nabla^2 c, \quad (18)$$

where $c \in [0, 1]$ is the concentration (phase field), $M = 1.0$ is the mobility coefficient, $\kappa = 0.357 \text{ J/m}$ is the gradient energy coefficient, and μ is the chemical potential. The bulk free energy density follows a regular solution model for Au-Pt alloy at temperature $T = 973.15 \text{ K}$:

$$f(c) = \frac{RT}{v_m} [c \ln c + (1 - c) \ln(1 - c)] + c(1 - c)[A_0 + A_1(1 - 2c)], \quad (19)$$

with $A_0 = 15000 + 6.1T$ and $A_1 = -7600 + 3.55T$. The spinodal decomposition process proceeds through three distinct phases: initial noise relaxation (0-20 Δt), rapid phase separation (20-600 Δt), and slow coarsening (>600 Δt) where the characteristic domain size grows over time.

The dataset is constructed on a periodic domain $[0, 128]^2$ discretized on a 128×128 grid for training and 1024×1024 for evaluation. The numerical solver uses explicit finite differences with $\Delta t = 0.01$. Initial conditions are generated as

$c_0 = 0.60 + 0.05 \times (\xi - 0.5)$ where $\xi \sim \mathcal{U}(0, 1)$ independently at each grid point. Due to the spatial self-similarity of spinodal decomposition, we employ a one-shot learning paradigm: training uses a single long trajectory rather than many short trajectories. All three stride models ($10\Delta t$, $100\Delta t$, and $1000\Delta t$) share the same training set: a single trajectory evolved from $t = 2000$ to $t = 52000\Delta t$, with snapshots saved every $10\Delta t$. Test evaluation uses 20 trajectories with different random seeds, extended to $t = 102000\Delta t$.

The three FluxNet-D models use ResNet backbones with 32 base channels but different configurations to accommodate their respective temporal strides. The $10\Delta t$ model uses 4 residual blocks with kernel size 3 and a 3×3 transport neighborhood. The $100\Delta t$ model uses 4 blocks with kernel size 5 and a 5×5 neighborhood. The $1000\Delta t$ model uses 6 blocks with kernel size 7 and a 9×9 neighborhood. All models are trained for 100 epochs with DCL weight $\gamma = 1.0$.

The two-point correlation function $S_2(\mathbf{r})$ quantifies the probability that two points separated by vector \mathbf{r} belong to the same phase. It is computed via FFT-based autocorrelation as $S_2(\mathbf{r}) = \langle \phi(\mathbf{x})\phi(\mathbf{x} + \mathbf{r}) \rangle_{\mathbf{x}}$, and the radial average $\bar{S}_2(r)$ provides a one-dimensional summary capturing the characteristic length scale of the microstructure. The first zero crossing of $\bar{S}_2(r)$ corresponds approximately to the mean domain size. We evaluate the MAE between predicted and reference radial correlations as a statistical accuracy metric that complements pointwise error.

The evaluation protocol proceeds as follows. We generate 100 random initial conditions on a 1024×1024 grid. Each initial condition is evolved to $t = 2000\Delta t$ using the phase-field solver to reach the early spinodal decomposition stage, which we denote as $t = 0T$ where $T = 50000\Delta t$ represents the temporal extent of the training data. From this starting point, the trained models propagate forward to $t = 2T$ (corresponding to $t = 102000\Delta t$ from the initial random state). Every $1000\Delta t$, we compute the two-point statistics error between model predictions and the phase-field reference. As a baseline for inherent statistical variability, we compute the correlation function difference between two independent phase-field simulations initialized with different random noise.

We perform gradient-based effective receptive field (ERF) analysis to verify that FluxNet-D operates as a local transport operator despite its potentially large theoretical receptive field. For each output channel c at spatial location (y, x) , we compute the gradient magnitude $G_c(y, x) = |\partial f_c(y, x) / \partial \mathbf{X}|$, where $f_c(y, x)$ is the channel output before the conservative update and \mathbf{X} is the input concentration field. We sample inputs from the test dataset to ensure relevance to learned dynamics: 10 random images are selected from the test set, and for each image, 10 random spatial locations are sampled (excluding boundary margins). Gradient maps are computed for all sampled locations, averaged across samples, and normalized by the maximum value. The effective receptive field is defined as pixels where the normalized gradient exceeds 1% of the maximum, and ERF size is computed as the square root of the pixel count. The theoretical receptive field for a backbone with initial convolution of kernel size k followed by B residual blocks (each with two $k \times k$ convolutions) is $\text{TRF} = k + 2B(k - 1)$.

Figure 9 compares phase field snapshots at four key time points ($0T, 1T, 1.5T, 2T$) between ground truth and all three FluxNet-D models. All models produce visually realistic microstructures with appropriate domain morphology and characteristic length scales that grow over time consistent with coarsening dynamics. The absolute error maps at the final time $2T$ reveal that prediction discrepancies are primarily concentrated in multiple localized regions. This pattern is characteristic of the branching phenomenon in chaotic dynamics: small prediction errors near interfaces can lead to divergent coarsening pathways (e.g., whether two adjacent domains merge or remain separate), while the overall statistical properties of the microstructure remain correct.

Figure 10 plots the radial two-point correlation function $\bar{S}_2(r)$ at four key times, comparing ground truth with all three models. The correlation functions show excellent agreement at all times. The characteristic length scale, indicated by the first zero crossing, is correctly captured by all models and grows appropriately over time.

Figure 11 tracks the phase volume fractions over time, defined as the fraction of pixels with $\phi \geq 0.6$ (high-concentration phase) and $\phi < 0.6$ (low-concentration phase). All FluxNet-D models accurately reproduce the phase fraction evolution, with predicted curves closely tracking the ground truth throughout the $2 \times$ extrapolation regime. This confirms that the conservation constraint enforced by the FluxNet architecture successfully maintains the global composition balance, translating to correct mass partitioning between phases at the macroscopic level.

Figures 12 and 13 visualize the ERF patterns for the $100\Delta t$ and $1000\Delta t$ models respectively (the $10\Delta t$ model ERF is shown in Figure 5 of the main text). As expected, models trained with larger time steps exhibit proportionally larger effective receptive fields: ERF sizes are approximately 9.7×9.7 pixels for $10\Delta t$, 12.2×12.2 for $100\Delta t$, and 19.0×19.0 for $1000\Delta t$. Importantly, all models maintain ERF sizes substantially smaller than their theoretical maximum receptive fields: the ERF/RF utilization ratios are 26.0%, 10.8%, and 5.8% for the three models respectively. This confirms that FluxNet-D

learns genuinely local transport operators rather than global convolutional mappings, supporting the physical interpretation of the learned dynamics as local mass transport between neighboring cells.

Figure 14 compares wall-clock time for completing $50,000\Delta t$ of simulation across domain sizes ranging from 256^2 to 4096^2 grid points. The GPU-accelerated phase-field solver time scales with both domain size (due to increased computation per step) and the fixed number of required time steps. In contrast, FluxNet-D inference time is dominated by the reduced number of forward passes: the $10\Delta t$ model requires 5,000 forward passes, the $100\Delta t$ model requires 500, and the $1000\Delta t$ model requires only 50. At the training resolution of 1024^2 , the $10\Delta t$ model is actually slower than the solver ($0.55\times$ speedup) due to inference overhead, but the $100\Delta t$ model achieves $3.81\times$ speedup and the $1000\Delta t$ model achieves $17.3\times$ speedup. The efficiency advantage of the coarser-timestep models increases at larger domain sizes because the fixed overhead per inference step becomes negligible compared to the savings from reduced step count.

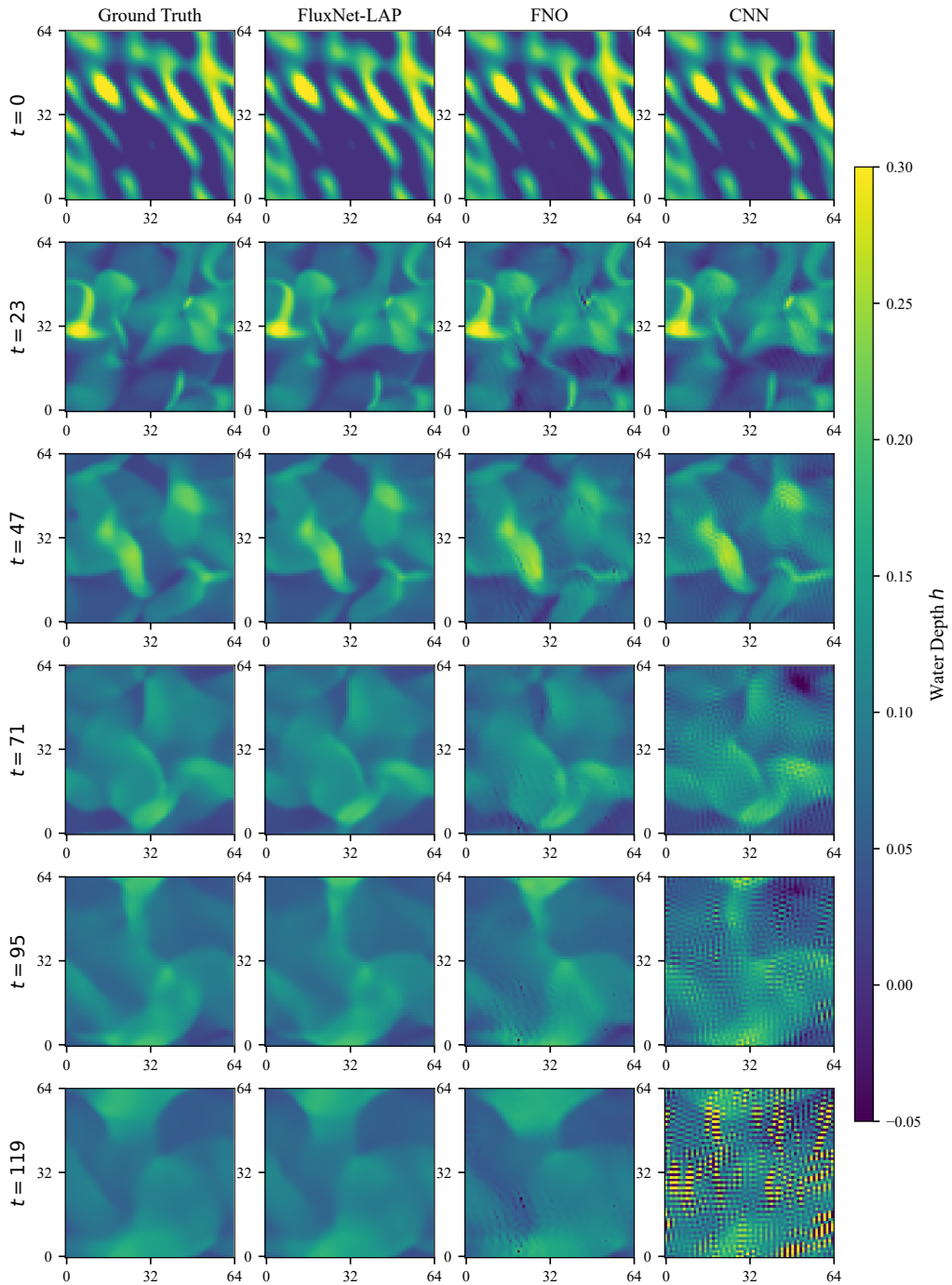


Figure 6. Time evolution of the water depth field $h(x, y, t)$ comparing ground truth, FluxNet-LAP, FNO, and CNN at six time steps spanning the rollout horizon.

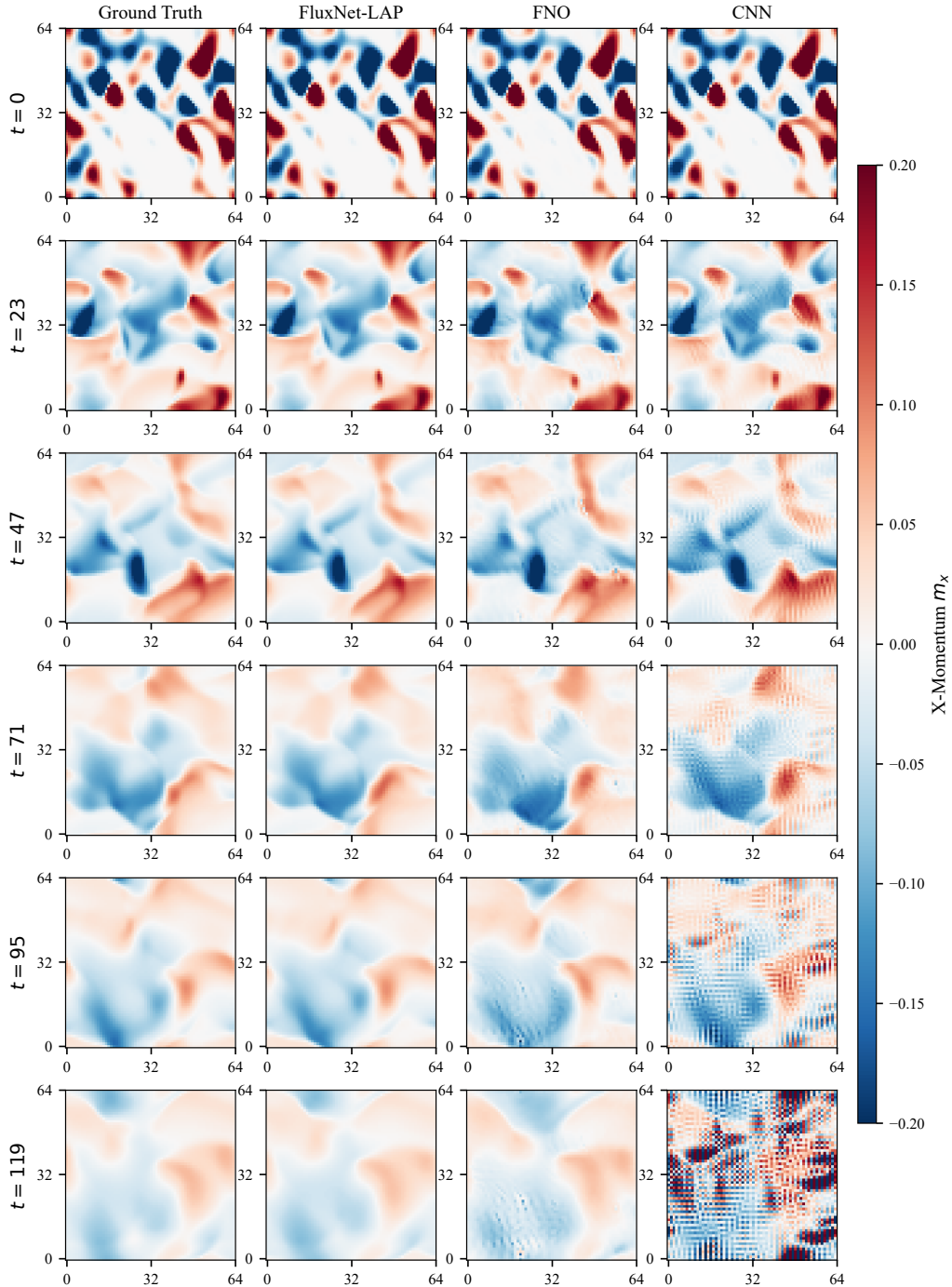


Figure 7. Time evolution of the x-momentum field $m_x(x, y, t)$ comparing ground truth, FluxNet-LAP, FNO, and CNN at six time steps. FluxNet-LAP maintains accurate predictions throughout, while CNN develops high-frequency artifacts.

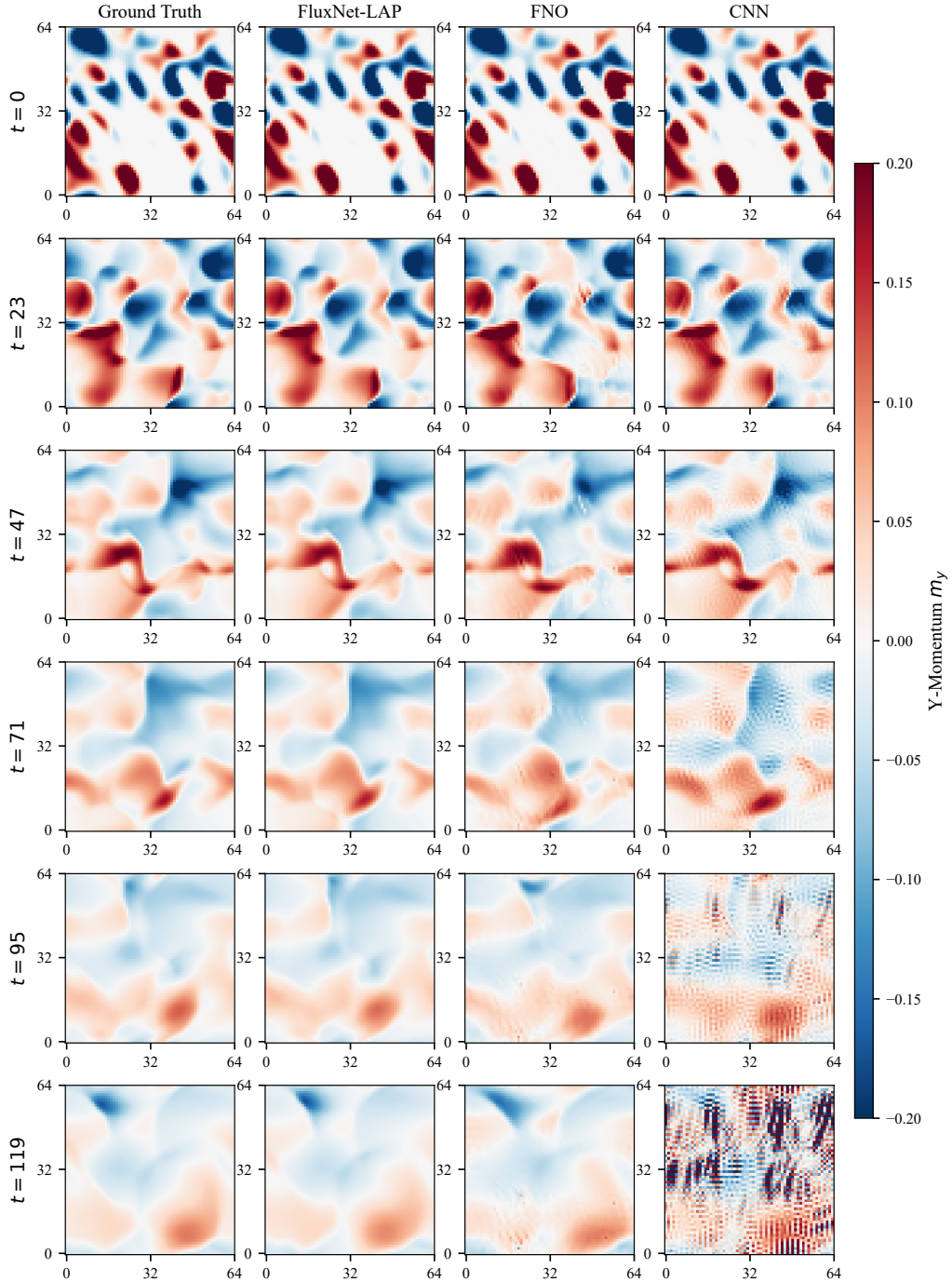


Figure 8. Time evolution of the y-momentum field $m_y(x, y, t)$ comparing ground truth, FluxNet-LAP, FNO, and CNN at six time steps. Similar patterns to m_x are observed, with FluxNet-LAP providing the most accurate predictions.

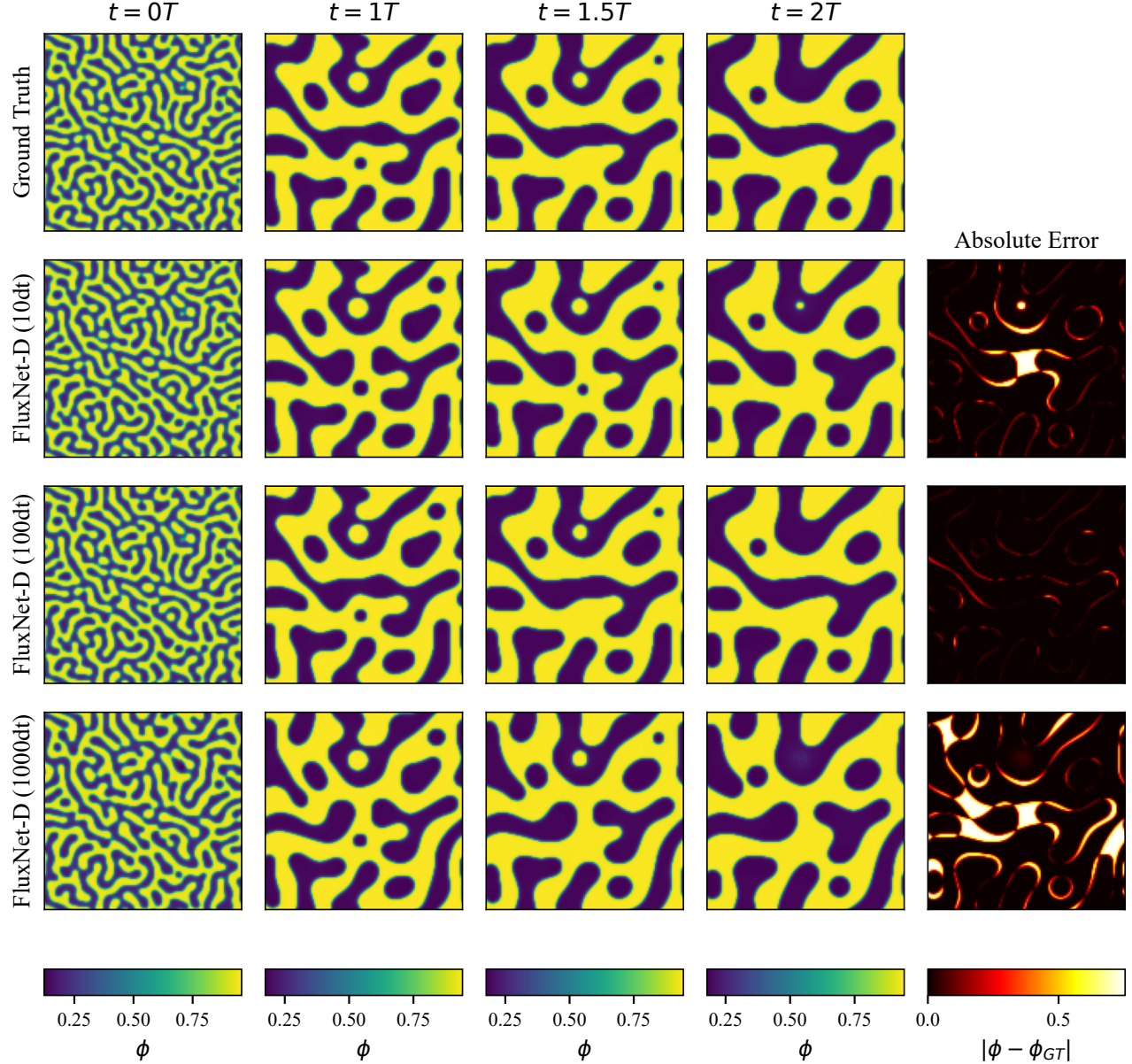


Figure 9. Phase field $\phi(x, y, t)$ evolution comparing ground truth and FluxNet-D models trained with different time step sizes ($10\Delta t, 100\Delta t, 1000\Delta t$) at four time points ($0T, 1T, 1.5T, 2T$). The rightmost column shows absolute prediction error at the final time $2T$.

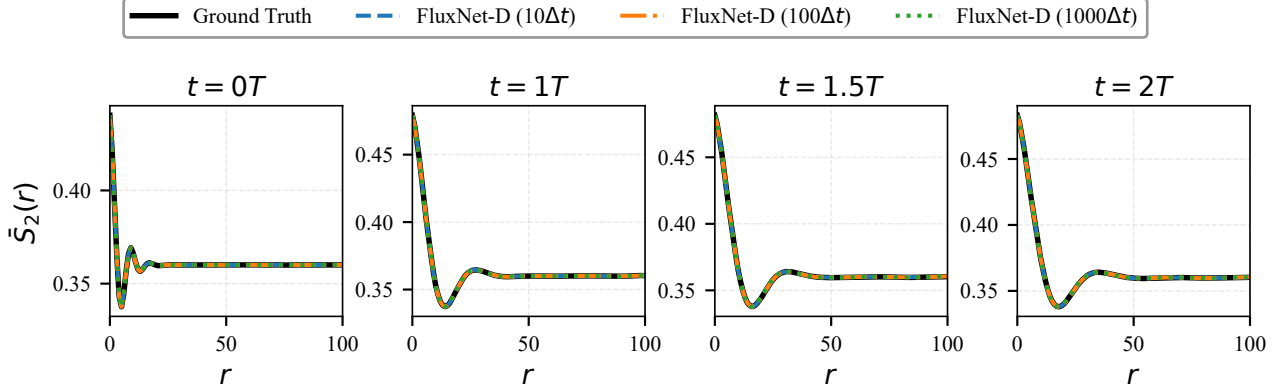


Figure 10. Radial two-point correlation function $\bar{S}_2(r)$ comparison between ground truth (phase-field simulation) and FluxNet-D models at four time points: $0T$ (initial), $1T$ (training horizon), $1.5T$, and $2T$ ($2\times$ extrapolation). All models closely match the reference correlation functions throughout the extrapolation regime.

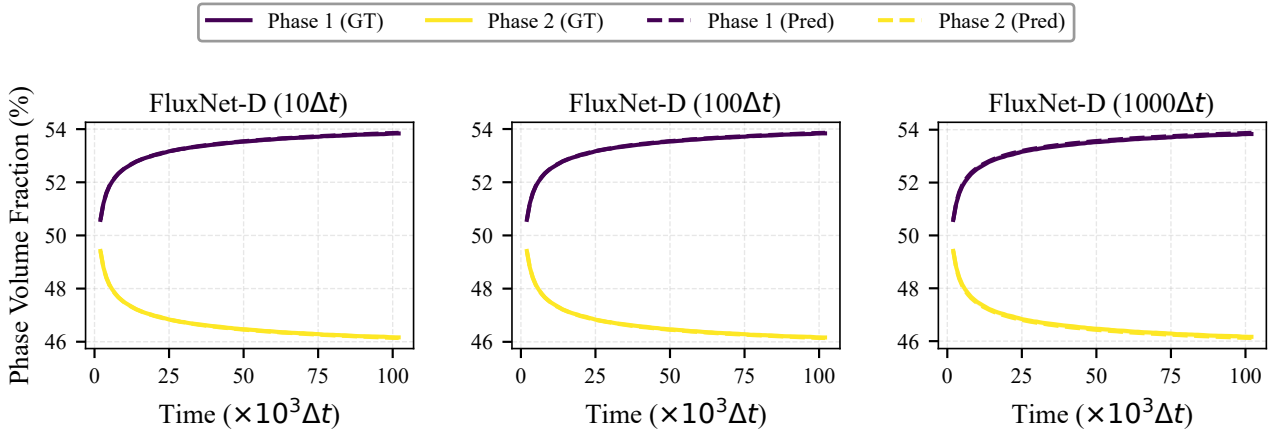


Figure 11. Phase volume fraction evolution during spinodal decomposition. Solid lines represent ground truth (phase-field simulation), dashed lines represent FluxNet-D predictions for models trained with different time step sizes. All models accurately track the evolution of both high-concentration ($\phi \geq 0.6$) and low-concentration ($\phi < 0.6$) phase fractions.

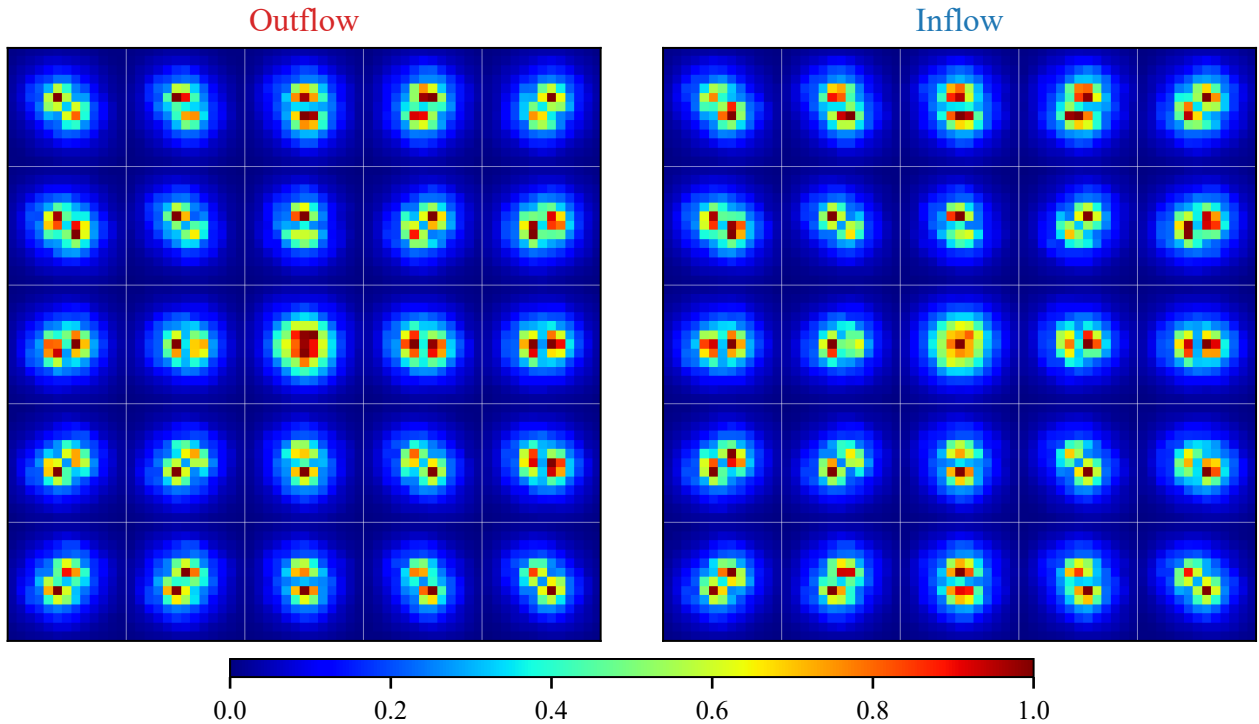


Figure 12. Effective receptive field (ERF) analysis for FluxNet-D trained with $100\Delta t$ time steps. Left panel: outflow branch channels arranged according to spatial offset indices within the 5×5 neighborhood. Right panel: inflow branch channels. The larger ERF compared to the $10\Delta t$ model (Figure 5 in main text) reflects extended transport range at coarser temporal resolution.

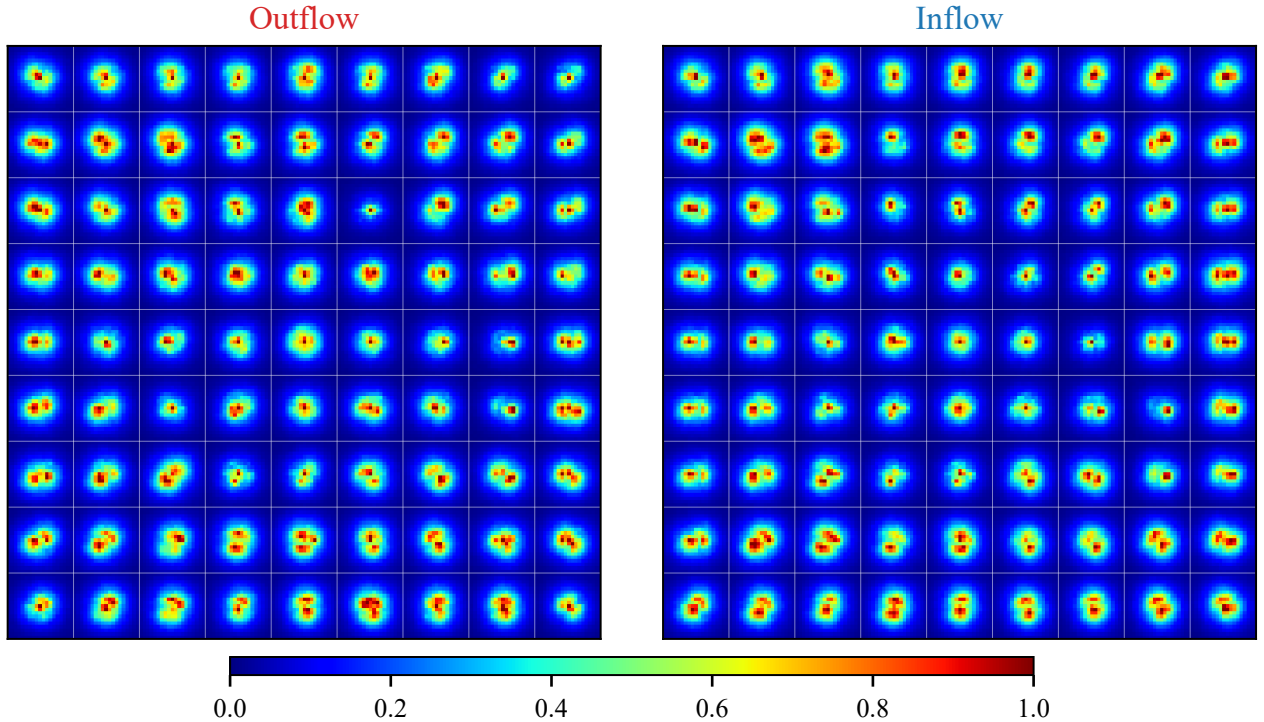


Figure 13. Effective receptive field (ERF) analysis for FluxNet-D trained with $1000\Delta t$ time steps. Left panel: outflow branch channels within the 9×9 neighborhood. Right panel: inflow branch channels. This model exhibits the largest ERF among the three variants, consistent with the extended spatial dependencies required for accurate prediction at the coarsest temporal resolution.

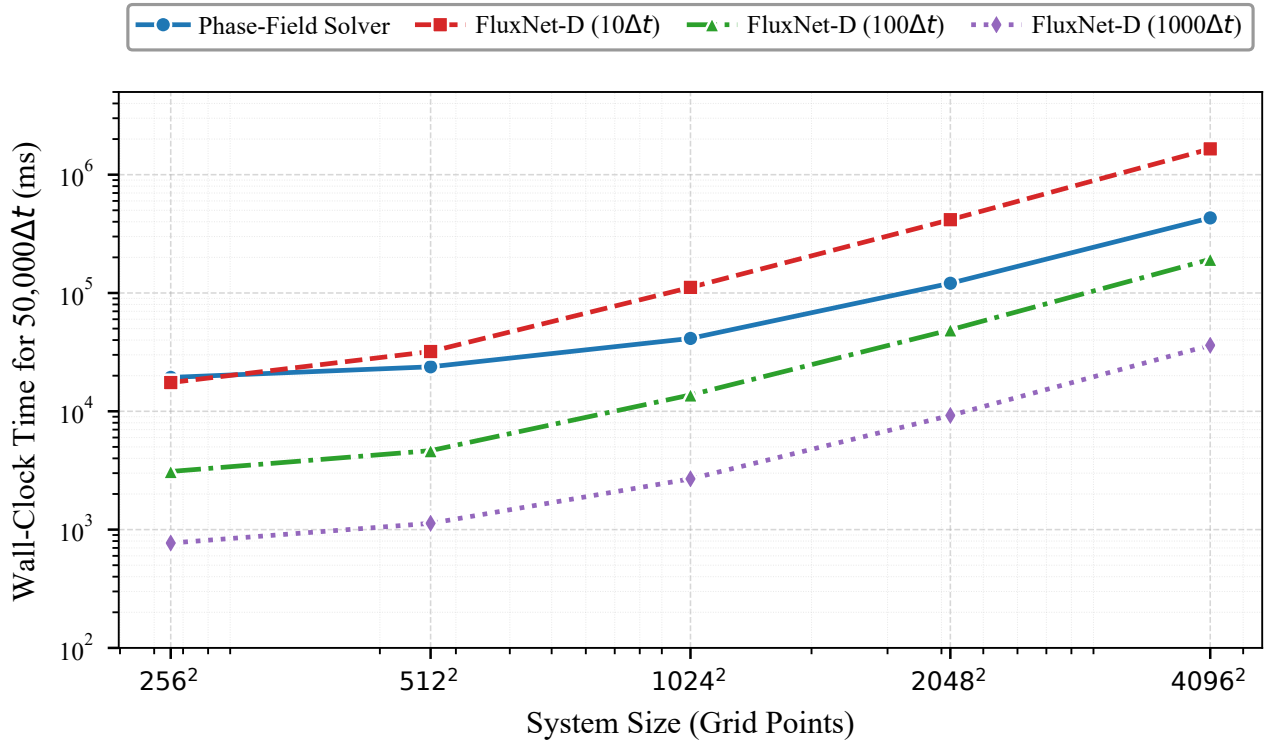


Figure 14. Wall-clock time comparison for completing $50,000\Delta t$ of spinodal decomposition simulation. Comparison between the GPU-accelerated phase-field solver and FluxNet-D models at three temporal resolutions across system sizes from 256^2 to 4096^2 grid points. Both axes use logarithmic scales. The $1000\Delta t$ model achieves $17.3\times$ speedup at 1024^2 resolution, with efficiency gains increasing at larger domain sizes.